TWO CHANNEL RECEIVER DESIGN AND IMPLEMENTATION FOR A GROUND BASED MICRO-PULSE DIFFERENTIAL ABSORPTION LIDAR (DIAL) INSTRUMENT

by

Drew Roland Moen

A thesis submitted in partial fulfillment
of the requirements for the degree

of

Master of Science

in

Electrical Engineering

MONTANA STATE UNIVERSITY
Bozeman, Montana

August, 2016

ACKNOWLEDGEMENTS

I would like to thank my family for all their support and understanding of my busy schedule and short notice planning habits, and Sarah Mondl for standing by me and offering support when nothing seemed to be going in our favor. I would like to thank my advisor, Dr. Kevin Repasky for providing this unique project. Thank you for allowing me to test my ideas in resolving many complications and giving insight on how to overcome those issues when I came back empty handed. Thanks also to Dr. John Carlsten for always offering an open door with someone to bounce ideas off of, to Dr. Paul Nachman for showing me how to dig further into the theory when I couldn't seem to make improvements to the extent that I hoped, to Dr. Wataru Nakagawa for staying around long after everyone else had left with an open door and advice to give when I'm stuck and otherwise on my own for the night, and to Dr. Joe Shaw for use of his lab space and for the upkeep of his radiosonde station by his research group. Thanks to Dr. Amin Nehrir for all his work on this project prior to my involvement, and for remaining available to help, and to Dr. Raymond Weber for always finding time to help resolve my particularly infuriating programming issues. Thanks to Chat Chantjaroen and Ben Soukup for their help around the lab and advice when working through some of my more difficult problems, and to all my friends for making our time spent in Bozeman immensely enjoyable.

This work was supported by the National Science Foundation grant number 1206166. Any opinions, findings, or conclusions expressed herein are those of the author and do not necessarily reflect the views of NSF.

TABLE OF CONTENTS

1. INTRODUCTION 1

The Earth's Atmosphere and Atmospheric Water Vapor 1
Water Vapor Measurement Techniques.....2
Thesis Organization 7

2. THEORY 8

Description of DIAL Technique 8
Derivation of DIAL Equation 9
Normalized Relative Backscatter Equation 15
Calculation of Water-Vapor Absorption Cross Section.....17

3. WATER-VAPOR DIAL INSTRUMENT 21

Transmitter.....21
Receiver 26
Ray Tracing Model of the Two Channel Receiver 28
Zemax Model of the Two Channel Receiver.....32
Programming for Autonomous Deployment 39

4. EXPERIMENTAL RESULTS.....42

Data Collection Summary.....42
Far Field Verification.....43
Near Field Verification 46

5. CONCLUSION.....54

REFERENCES CITED.....58

LIST OF FIGURES

Figure Page

1.1 The primary layers of the Earth's atmosphere 1

3.1 Schematic diagram of the DIAL laser transmitter 21

3.2 Schematic diagram of the DIAL receiver 27

3.3 Layout of the optical model for the near field receiver using ABCD matrices showing M_1 through M_9 from left to right. The value "h" represents the distance from the reflecting particle to the telescope and was scanned from 0 to 12 kilometers. 29

3.4 Plot of beam radius at the fiber input versus beam altitude for various offset distances between the fiber input and the focus of the fiber coupling lens. 30

3.5 Plot of maximum beam angle seen at the fiber versus beam altitude with maximum allowable beam angle shown by the red dashed line. 31

3.6 Plot of beam radius at the near field detector input versus beam altitude for various offset distances between the detector and the focus of the detector focusing lens. 32

3.7 Zemax lens diagram model for a) telescope, b) far field channel, and c) near field channel. 33

3.8 Comparison of ray tracing model to Zemax model of beam radius vs range measured after collimation of the light through the telescope. 34

3.9 Comparison of ray tracing model to Zemax model of maximum ray angle vs range measured after collimation of the light through the telescope. 35

3.10 Comparison of ray tracing model to Zemax model of beam diameter vs range measured at the location of the fiber. 36

3.11 Comparison of ray tracing model to Zemax model of maximum ray angle vs range measure at the location of the fiber. 37

LIST OF FIGURES – CONTINUED

Figure Page

3.12 Comparison of ray tracing model to Zemax model of beam radius vs range measured at the near field detector. 38

3.13 Screen shot of the user interface for the scalar card program which shows a live feed of the raw data return 39

3.14 Screen shot of the user interface used to set the wavelength while observing a live feed of measurements such as water vapor and NRB 40

4.1 A plot of the measured normalized relative backscatter ranging from July 17th 2013 through July 27th 2013..... 43

4.2 A plot of the measured water vapor number density ranging from July 17th 2013 through July 27th 2013..... 44

4.3 Four plots showing measured water vapor number density profiles in solid black compared to radiosonde data in dotted red at four different times during the data run in July 2013 45

4.4 A plot of the measured offline background counts per second from the far field channel ranging from August 1st 2015 to October 10th 2015..... 46

4.5 A plot of the column optical depth from the far field channel ranging from August 1st 2015 to October 10th 2015 47

4.6 A plot of the relative backscatter from the far field channel ranging from August 1st 2015 to October 10th 2015 47

4.7 A plot of the water vapor number density from the far field channel ranging from August 1st 2015 to October 10th 2015 48

4.8 A plot of the measured offline background counts per second from the near field channel ranging from August 1st 2015 to October 10th 2015..... 48

4.9 A plot of the column optical depth from the near field channel ranging from August 1st 2015 to October 10th 2015 49

LIST OF FIGURES – CONTINUED

Figure Page

4.10 A plot of the relative backscatter from the near field channel ranging from August 1st 2015 to October 10th 2015 49

4.11 A plot of the water vapor number density from the near field channel ranging from August 1st 2015 to October 10th 2015 50

4.12 A plot from June 30th 2016 at MST 9:17am showing the far field overlap decaying below 1.5 km and the near field overlap decaying below 1 km. 51

4.13 A profile from August 9th 2015 at MST 10:25pm showing good agreement between 1 km and 4.2 km. The far field continues producing reasonable data up to 5 km. 52

4.14 A profile from September 1st 2015 at MST 11:35am showing good agreement between 700 meters and 3 km. The far field continues producing reasonable data up to 4.7 km. 52

ABSTRACT

Current standard water vapor measurement techniques lack the required temporal and spatial resolution needed to further our understanding of the role of water vapor in the Earth's atmosphere. This thesis reports on the continued efforts to bring a cost-effective, autonomous, eye-safe, ground based, micro-pulse differential absorption lidar for the continuous measurement of water vapor into fruition. More specifically, the receiver for this instrument needs a dynamic range of measurement spanning from as close to the Earth's surface as possible, up through the troposphere. Previous reports on this system provide accurate backscatter measurement down to 2 km above the surface. A newly designed receiver has been modeled with the help of Zemax optical design software. It implements a 10% pickoff of the total received light into a second detection channel with a wider field of view. This channel utilizes a free space avalanche photodiode (APD) and has a full angle field of view of ~1 mrad. This channel (the near field) provides accurate backscatter measurement between 600 meters and 5 km in theory. The 90% channel utilizes a fiber coupled APD with a full angle field of view of ~200 μrad. This channel (the far field) has been shown to provide accurate backscatter measurements between 2 km and 12 km. While the near field channel has shown improvement to the overall system, the measured results appear to be accurate down to ~1 km. The results show continuous and autonomous operation with water vapor measurements in close agreement from both detection channels. Further comparisons with radio-sondes provide validation of the water vapor DIAL data product.

INTRODUCTION

The Earth's Atmosphere and Atmospheric Water Vapor

The Earth's atmosphere is defined by four main layers starting from the surface of the earth and ending at the vacuum of space. These layers from the ground up are the troposphere, stratosphere, mesosphere, and the thermosphere or ionosphere. These are bounded by the earth's surface, the tropopause, the stratopause, the mesopause, and the exosphere (edge of space where any residing molecules no longer behave as a gas) respectively. An illustration of these four main layers alongside their approximate height, atmospheric pressure, and temperature is shown in figure 1.1.

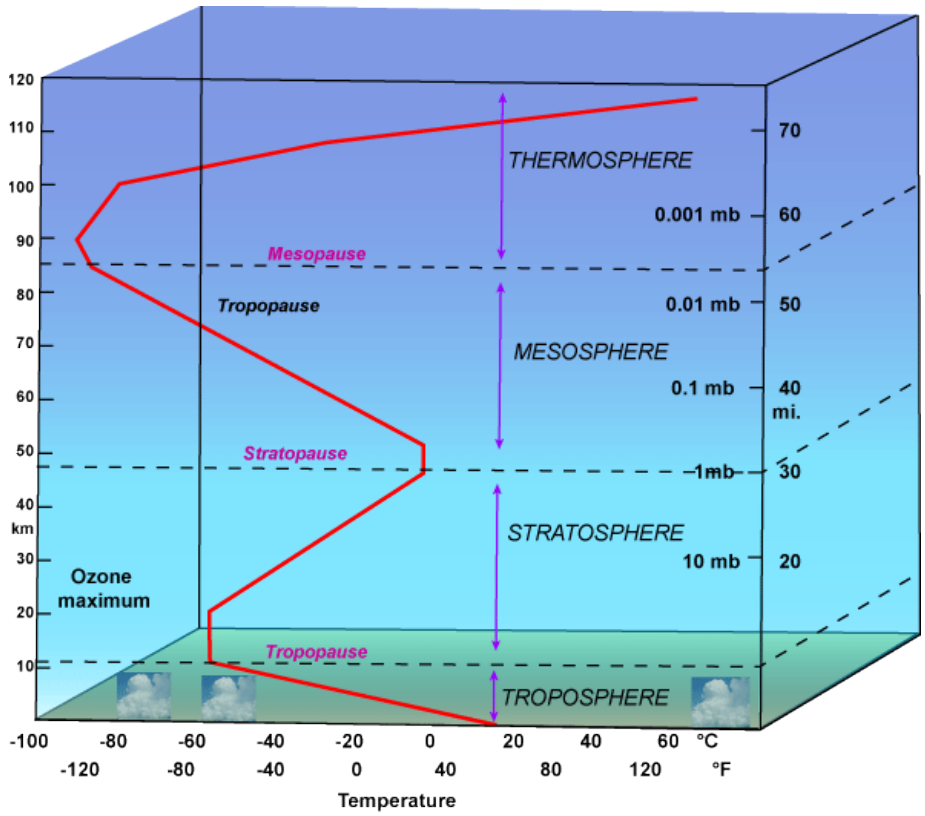

Figure 1.1: The primary layers of the Earth's atmosphere. [1]

Water vapor is important in many key atmospheric processes associated with both weather and climate such as i) the main component of clouds and rain, ii) a means of transporting energy via latent heat and iii) a regulator of temperatures via the greenhouse effect. The great variety of sources (evaporation) and sinks (condensation) causes it to vary widely in space and time. Approximately half of the atmospheric water vapor is below 2 km. These atmospheric processes involving water vapor are the most difficult to model. But all global circulation models (GCMs) must take into account the spatial and temporal variation of water vapor to properly account for it. Having long-term, high-resolution, vertical profiles of water vapor will help to monitor the water vapor structure and variability and its associated impact on weather and climate.

Water Vapor Measurement Techniques

Ground based measurements of water vapor, along with other important thermodynamic variables including temperature and pressure, are currently conducted using radiosonde measurements, which together with satellite based instruments, form the backbone of the observations used for weather forecasting. Radiosonde measurements are typically available twice each day from widely distributed spatial locations allowing weather forecasting of large scale features. However, because of the limited spatial and temporal observations, weather forecasting of high impact mesoscale events such as thunderstorms is limited [2]. Improved understanding of the water vapor structure and variability at the mesoscale will require observations from more densely spaced ground based sites that provide continuous time data and capture the vertical structure of the

lower atmosphere. A recent report by the National Research Council [3] lists high-resolution vertical profiles of humidity in the lower troposphere and planetary boundary layer height as two of the four highest priority observations that need to be addressed for improved mesoscale weather forecasting.

Improved measurements of water vapor are a long-standing observational challenge to the meteorological and climate research and forecasting community. Space-based satellite platforms housing passive sensors such as the Michelson Interferometer for Passive Atmospheric Sounding (MIPAS) [4], the Atmospheric Infrared Sounder (AIRS) [5], and the Halogen Occultation Experiment (HALOE) [6] have shown great utility for global coverage of water vapor fluxes but are limited to the upper troposphere and lower stratosphere region due to accessibility to various atmospheric windows. These sensors also suffer from coarse vertical resolution of 1- 6 km, and only provide limited temporal data at any one site based on the satellite orbit. The Atmospheric Emitted Radiance Interferometer (AERI) [7] is a passive ground based instrument that utilizes emitted radiance from the atmosphere to measure temperature and water vapor profiles. The AERI instrument relies on blackbody calibration and requires an initial guess at a temperature and water vapor profile. An iterative recursive physical solution to the radiative transfer equation is then conducted to yield a final temperature and water vapor profile. The microwave radiometer (MWR) [8, 9] is a second ground based instrument that utilizes radiance measurements with a statistical retrieval algorithm that uses monthly derived and location dependent linear regression coefficients. The MWR instrument requires calibration and has range dependent vertical resolution greater than

500 m for altitudes beyond 1 km [8, 9]. Although providing thermodynamic profiling of the atmosphere, including water vapor and temperature profiles, these two passive instruments require precise and difficult calibration methods including the use of cryogenics. The quality of these measurements rely heavily on the accuracy of the calibrations as well as the stability of the rigorous mathematical regressions and weighting functions used in the inversions.

Active remote sensing instruments such as lidar have become an attractive alternative to passive sensors for monitoring atmospheric gases and aerosols with high spatial and temporal resolution. The two main types of lidar used for profiling atmospheric water vapor include Raman lidar [10, 11, 12] and differential absorption lidar (DIAL) [13-25]. The Raman lidar technique uses the characteristic Raman shift in wavelength to measure range resolved profiles of gases including water vapor. Raman lidar instruments typically require a high power laser transmitter to compensate for the relatively small Raman scattering cross section and also require precise calibration using radiosonde or *in situ* measurements to maintain accurate water vapor profiles. Alternatively, the DIAL technique utilizes the elastic backscatter return signals from two different transmitted wavelengths to retrieve water vapor profiles, one associated with the center or side of an absorption feature and the other absent of any absorption features. Water vapor profiles are then retrieved using the ratio of the backscattered returns from the two closely spaced transmitted wavelengths. This method removes the instrument and atmospheric dependent calibration constants from the lidar equation and allows the retrieval of water vapor profiles using a straightforward equation and the differential

absorption cross section for water vapor, which can be measured in the laboratory under different temperature and pressure conditions, and have been tabulated in the HITRAN database [26].

Various research groups around the world have developed and deployed DIAL instruments for a wide range of measurements in various geographic locations. Airborne water vapor DIAL instruments (LASE [13], LEANDRE II [25], WALES [19]) have been developed and deployed at several field campaigns. Ground based scanning water vapor DIAL instruments have also been deployed at field campaigns such as the International H_2O Project (IHOP) [27] and the Convection and Orographically-induced Precipitation Study (COPS) [28]. These research grade DIAL instruments demonstrate the utility of water vapor profiling using active sensors, but because of their high cost, large footprint, extensive user interaction, and maintenance levels they do not lend themselves to deployment in a network -- such as would be required for mesoscale weather observations and forecasting.

In recent years, work has begun on developing smaller, automated, water vapor lidar instruments. Numerical studies of diode-laser-based transmitters and photon counting avalanche photodiode based receivers have been performed [29, 30], but few systems have been built. Rall et al. [14] demonstrated initial results from a DIAL instrument using a psuedonoise code modulated diode laser near 810 nm. Machol et al. (CODI) [20] reported initial water vapor DIAL measurements using a laser transmitter based on a distributed feedback (DFB) laser diode used to injection seed a flared amplifier. Comparisons between CODI's DIAL retrievals and radiosonde measurements

showed moderate agreement up to a height of 2.5 km above ground level. Machol et al. [20] noted that new laser transmitter designs are needed for better spectral coverage and larger tuning ranges, calling for a new laser with a tuning range to access a larger selection of water vapor lines and allow for operations in various geographic locations.

Recently, researchers at Montana State University (MSU) demonstrated a micro-pulse DIAL instrument using semiconductor based technology for water vapor and aerosol profiling in the lower troposphere [21-24]. They utilized advances in commercially available tapered semiconductor optical amplifiers (TSOA's) to produce a widely tunable laser transmitter capable of accessing many water vapor absorption lines in the 830 nm band. The instrument was constructed primarily from commercial off-the-shelf (COTS) components and was the first diode-laser based DIAL to demonstrate both day and night profiling capabilities of water vapor. The laboratory performance, coupled with a low-cost and compact design, suggests the instrument has potential to fill the need described by the National Research Council [3] for high-resolution vertical profiles of water vapor in the lower troposphere and boundary layer height monitoring needed for the next generation mesoscale weather observation network.

The work presented in this thesis describes the fourth generation water vapor DIAL instrument designed and built in the Applied Optics and Remote Sensing (AORS) laboratory at MSU. The major improvements to the instrument include the incorporation of a near field and far field channel in the receiver. The use of two detection channels is important in order to achieve full overlap of the receiver from as close to the ground as possible through the troposphere, where overlap refers to the percentage of the light

captured by the telescope that is then focused onto the detector. Full overlap simply implies the case where 100% of the light reflecting from a specific altitude is observed by the detector. The near field channel utilizes a free space avalanche photodiode (APD) that provides a wide field of view allowing full instrument overlap to occur starting at 1 km. The far field channel utilizes a fiber coupled APD with a narrow field of view that comes into full overlap at approximately 2 km. The necessity of this narrow field of view for the far field channel lies with its ability to reject enough background noise to make accurate measurements through the upper troposphere where very low return signal is achieved. This two channel receiver allows water vapor and aerosol profiles to be obtained between 500 m and 4 km during daytime operations and 500 m and 6 km during nighttime operations.

Thesis Organization

This thesis is organized as follows. Chapter 2 describes the theory used in the calculations required to process the raw information collected by the DIAL instrument as well as some of the theory behind the choice in water vapor absorption feature. A description of the water vapor DIAL instrument and the theoretical modeling of the changes made to the receiver is contained in chapter 3. Chapter 4 presents the experimental results that were observed upon completion of the newly designed receiver. A summarization, some concluding remarks and the future work for the DIAL system are found in chapter 5.

THEORY

Description of DIAL Technique

Lidar, Light Detection and Ranging, is a remote sensing technique used to gather information about materials found in the atmosphere such as the microphysical structure, amount, or spectroscopic features of atmospheric particles or molecules. This is achieved by transmitting short, coherent, collimated light pulses into the atmosphere. The pulses of light can be absorbed or scattered by aerosols, particulates, and molecules that are found in the flight path. A small fraction of the scattered light is backscattered (scattered 180 degrees off the scatter material) into a receiver telescope, which sends the light to be filtered around the wavelength of interest, adjusted for the purpose of the measurement if needed, and detected with a photo-multiplier tube (PMT), or an avalanche photo diode (APD). A data acquisition (DAQ) card digitizes the detected light, while separating the data into range-specific bins. These range bins are filled with data one at a time since the time of detection is proportional to the distance traveled by each detected photon.

The purpose of a differential absorption lidar (DIAL) is to measure the range-resolved number density of a molecule of interest. The received power of a lidar system is described with the lidar equation, which can be used to derive the DIAL equation. There are two assumptions made when considering the general lidar equation. The first assumption is that scattering events are independent. This means that particles and molecules found in the atmosphere move around in a random fashion with enough space in between scatterers that any phase relation will be lost in the return signal. The second

assumption is that any detected photon was only scattered once during its entire time of flight, which is a reasonable assumption due to the already low probability of back reflection occurring. This is an important assumption necessary for resolving the range from which that photon was scattered.

Derivation of DIAL Equation

The general lidar equation is shown by equation 2.1 and is the starting point in the derivation of the DIAL equation. The received power, $P_R(\lambda, r)$ [W], at wavelength λ and from a distance r, is calculated with the lidar equation [31]

$$P_R(\lambda, r) = P_T(\lambda_T) * \Delta R * \beta(\lambda, \lambda_T, r, \theta) * \frac{A}{r^2} * T_T(\lambda_T, r)\, T_R(\lambda, r) * \eta(\lambda)\, O(r) + P_B \quad (2.1)$$

where $P_T(\lambda_T)$ [W] is the power out of the transmitter at the transmitted wavelength λ_T. ΔR [m] is the range bin as set by the laser pulse duration τ [s] and the speed of light $c = 2.998 * 10^8$ [m/s] using the equation, $\Delta R = \tau c/2$. $\beta(\lambda, \lambda_T, r, \theta)$ [$m^{-1}sr^{-1}$] is a volume scatter coefficient at a distance r for an angle θ between the direction of laser propagation and the telescope center axis. This is dependent on both the transmitted wavelength λ_T, and the received wavelength λ, which can change during processes such as Raman scattering. The type of scatter and probability of occurrence over the illuminated volume bounded by ΔR is accounted for by this value. A [m^2] is the surface area of the receiver telescope. It can be shown that this area divided by the square of the distance will provide the solid angle [sr] formed from the scatter site to the telescope.

$\mathrm{T_T}(\lambda_T, r)$ [unitless] and $T_R(\lambda, r)$ [unitless] are the transmissions over distance r for the outgoing transmitted light and the incoming return light respectively. $\eta(\lambda)$ [unitless] is the overall optical efficiency of the receiver. This encompasses the transmission for each element within the receiver, as well as the detector efficiency. $O(r)$ [unitless] is the geometric overlap factor for the receiver. P_B [W] is the background power produced by the detector which provides the power seen due to solar background noise and detector noise.

Two more assumptions can be made to help simplify the general lidar equation for our purposes. By assuming a co-linear configuration, the angle dependence can be dropped making note that θ=180° for the backscatter coefficient. Since differential absorption lidar doesn't rely on a frequency shift during the scattering process, elastic scattering can be assumed or $\lambda = \lambda_T$. Equation 2.1 can then be simplified to the Equation 2.2.

$$P_R(\lambda, z) = P_T(\lambda) * \Delta R * \beta(\lambda, \mathrm{z}) * \frac{A}{z^2} * \mathrm{T}(\lambda, z)^2 * \eta(\lambda)\, O(z) + P_B \qquad (2.2)$$

Since typical returns are on the order of individual photons for micro-pulse instruments such as described in this thesis, another useful form for this equation is in terms of photon counts (N_R, N_T and N_B). These variables can be directly exchanged with the power variables (P_R, P_T, and P_B). Since the transmitted power is typically observed in Watts, N_T can be written in terms of power using the equation $N_T = P_T(\lambda)\lambda\tau/(hc)$ [number of photons] where $h = 6.626 * 10^{-34}$ [J·s] is Plank's constant.

The atmospheric transmission factor (T^2) can be expressed using the Beer Lambert relationship as shown by equation 2.3. [31]

$$T(\lambda, z)^2 = \exp\left(-2\int_0^z \alpha(\lambda, z')dz'\right) = \exp\left(-2\int_0^z \kappa(\lambda, z')dz'\right)\exp\left(-2\int_0^z \sigma(\lambda, z')N(z')dz'\right) \tag{2.3}$$

The total atmospheric extinction coefficient, $\alpha(\lambda, z')$ [m^{-1}], can be expanded as the sum of the atmospheric extinction factor due to scattering, $\kappa(\lambda, z')$ [m^{-1}], and the atmospheric extinction factor due to absorption, $\sigma(\lambda, z')N(z')$ [m^{-1}]. The sum of these terms can then be separated into two exponential terms which is also shown in equation 2.3. $\sigma(\lambda, z')$ [m^2] is the absorption cross section associated with the molecule of interest, and $N(z')$ [m^{-3}] is the number density in molecules per unit volume. The retrieval of the number density is the goal of the DIAL instrument.

For any DIAL instrument, an appropriate absorption feature must be chosen. This instrument is a continuation of the system already developed at Montana State University. [24] The water vapor absorption feature was chosen in the 830 nm spectral region due to the existence of commercially available TSOAs and laser diodes at that wavelength. This wavelength also provides a target range covering the entire troposphere. Line strength and temperature dependence were also considered when choosing the feature at 828.187nm. [24]

The water vapor absorption line chosen to make the differential measurement has a center wavelength of 828.187nm (vacuum), a line-strength of 1.64×10^{-23} cm^{-1}/(molecule cm^{-2}), a full width at half maximum (FWHM) pressure broadened linewidth at sea level of 0.1896 cm^{-1} (2.1pm, 0.9 GHz), a linewidth temperature dependence of 0.74 and a ground state transitional energy of 212.1564 cm^{-1}. [24, 26, 32]

The DIAL technique utilizes two laser sources which are closely spaced in wavelength. One laser is tuned on the absorption feature of a molecule of interest (online). The other laser (offline) is far removed from the absorption feature so that the loss in signal due to molecular absorption is much less then that seen by the online laser. Using these two laser wavelengths, the number density of the molecule of interest can be retrieved from the backscatter measurements of the two laser wavelengths.

Two assumptions can be made to calculate the molecular number density. First, it must be assumed that the scatter profile seen at the online wavelength is equivalent to the profile seen at the offline wavelength. This means the samples taken from each laser were taken from the same volume of molecules. This is a reasonable approximation if we alternate the transmission between lasers at a quick enough rate. The second assumption that can be made is that the two lasers are still close enough in wavelength that the optical setup and scattering due to aerosols and other molecules is the same for each, leaving only the absorption due to the molecule of interest as the reason for change between the two signals. This can be a reasonable assumption given an appropriate absorption cross section. Under this assumption, the terms shown in equations 2.4a)-c) can be simplified as shown.

$$\beta(\lambda_{on}, z) = \beta(\lambda_{off}, z) = \beta(z) \tag{2.4a}$$

$$\eta(\lambda_{on})O(z) = \eta(\lambda_{off})O(z) = \eta O(z) \tag{2.4b}$$

$$\kappa(\lambda_{on}, z) = \kappa(\lambda_{off}, z) = \kappa(z) \tag{2.4c}$$

With the end goal of solving for the number density in mind, equation 2.2 can be used to compare the return power over a range bin of size Δz. The background noise can be subtracted off during lidar operation by taking measurements beyond the range at which all return signal is lost due to extinction. These measurements will directly show the noise floor which is approximately equal across all range bins. With the background noise subtracted off, a ratio of the observed power at location z and $z + \Delta z$ can be made as shown in equation 2.5. This can be simplified to equation 2.6 by substituting in equation 2.3.

$$\frac{P_R(\lambda, z)}{P_R(\lambda, z + \Delta z)} = \frac{P_T(\lambda) * \Delta R * \beta(\lambda, z) * \frac{A}{z^2} * T(\lambda, z)^2 * \eta(\lambda)\, O(z)}{P_T(\lambda) * \Delta R * \beta(\lambda, z + \Delta z) * \frac{A}{z^2} * T(\lambda, z + \Delta z)^2 * \eta(\lambda) O(z + \Delta z)} \tag{2.5}$$

$$\frac{P_R(\lambda, z)}{P_R(\lambda, z + \Delta z)} = \frac{\beta(\lambda, z) O(z) \exp\left(-2 \int_0^z \kappa(\lambda, z') dz'\right) \exp\left(-2 \int_0^z \sigma(\lambda, z') N(z') dz'\right)}{\beta(\lambda, z + \Delta z) O(z + \Delta z) \exp\left(-2 \int_0^{z+\Delta z} \kappa(\lambda, z') dz'\right) \exp\left(-2 \int_0^{z+\Delta z} \sigma(\lambda, z') N(z') dz'\right)} \tag{2.6}$$

The exponentials can be combined by noting that only the bounds on the integrals will be changed, resulting in equation 2.7.

$$\frac{P_R(\lambda,z)}{P_R(\lambda,z+\Delta z)} = \frac{\beta(\lambda,z)O(z)}{\beta(\lambda,\mathrm{z}+\Delta\mathrm{z})O(\mathrm{z}+\Delta\mathrm{z})} * \exp\left(2\int_z^{z+\Delta z}\kappa(\lambda,z')dz'\right)\exp\left(2\int_z^{z+\Delta z}\sigma(\lambda,z')N(z')dz'\right) \quad (2.7)$$

Equation 2.7 can be used to take a ratio between the online and offline wavelengths over the same range bin as shown in equation 2.8. On this step it is noted that many terms cancel due to the assumptions made from equations 2.4a-c.

$$\frac{\frac{P_R(\lambda_{on},z)}{P_R(\lambda_{on},z+\Delta z)}}{\frac{P_R(\lambda_{off},z)}{P_R(\lambda_{off},z+\Delta z)}} = \frac{\exp\left(2\int_z^{z+\Delta z}\sigma(\lambda_{on},z')N(z')dz'\right)}{\exp\left(2\int_z^{z+\Delta z}\sigma(\lambda_{off},z')N(z')dz'\right)} \quad (2.8)$$

This can be further simplified by assuming that the range bins are small enough that the number density and the absorption cross section are approximately constant over the range bin. This assumption sets the two integrals equal to the bin size, Δz, as shown by equation 2.9.

$$\frac{P_R(\lambda_{on},z)P_R(\lambda_{off},z+\Delta z)}{P_R(\lambda_{on},z+\Delta z)P_R(\lambda_{off},z)} = exp\left(2N(z)\Delta z\left(\sigma(\lambda_{on},z)-\sigma(\lambda_{off},z)\right)\right) \quad (2.9)$$

From here, the number density of the molecule of interest can be calculated. This is known as the DIAL equation and is shown by equation 2.10.

$$N(z) = \frac{1}{2\Delta z\left(\sigma_{on}(z) - \sigma_{off}(z)\right)}\left[\ln\left(\frac{P_R(\lambda_{on}, z)P_R\left(\lambda_{off}, z + \Delta z\right)}{P_R(\lambda_{on}, z + \Delta z)P_R\left(\lambda_{off}, z\right)}\right)\right] \quad (2.10)$$

Looking back at the assumption 2.4b, it is noted that some optics might still require wavelength dependence to be considered if the responsivity of the individual optic changes significantly between the online and offline wavelengths. Typical elements found in Lidar systems consist primarily of glass-based optics or mirrors, which can be assumed to have a constant responsivity over the online and offline wavelength range. The receiver, however, must implement narrowband filtration in an effort to reduce the background noise on the detector. If the filter is narrow enough, as it often will be, then the final DIAL equation will include an additional natural log term with narrow band filter transmission efficiencies $\eta_F(\lambda, z)$ [unitless] as functions of both wavelength λ and distance z. The DIAL equation with these filters considered is shown by equation 2.11. [24]

$$N(z) = \frac{1}{2\Delta z\left(\sigma_{on}(z) - \sigma_{off}(z)\right)}\left[\ln\left(\frac{P_R(\lambda_{on}, z)P_R\left(\lambda_{off}, z + \Delta z\right)}{P_R(\lambda_{on}, z + \Delta z)P_R\left(\lambda_{off}, z\right)}\right) - \ln\left(\frac{\eta_F(\lambda_{on}, z)\eta_F\left(\lambda_{off}, z + \Delta z\right)}{\eta_F(\lambda_{on}, z + \Delta z)\eta_F\left(\lambda_{off}, z\right)}\right)\right] \quad (2.11)$$

<u>Normalized Relative Backscatter Equation</u>

The lidar equation can be regrouped to form another important value known as the normalized relative backscatter (NRB). The NRB provides an idea of how much scatter material is in the atmosphere at each altitude. It is normalized to the constant

terms in the lidar equation and is range corrected to be relative to the amount of scattering regardless of the telescope field of view. The NRB is defined by equation 2.12 and can be described in terms of received and transmitted power using the lidar equation. [24]

$$NRB(\lambda, z) = \left(\Delta R * A * \eta(\lambda)\right) * \beta(\lambda, z, 180°) * T(\lambda, r)^2 = \frac{(P_R(\lambda, z) - P_B) * z^2}{P_T(\lambda) * O(z)} \tag{2.12}$$

The two main data products of the DIAL described in this thesis are the NRB and the number density ($N(z)$). According to the DIAL equation, in order to find the number density, all that is needed is a measurement of the power (number of photons) at each wavelength at a distance, z, with a width of Δz. The two cross section values are known by using HITRAN, described in more detail below, and any necessary filter efficiencies can be either calculated based on their specifications, or found through laboratory based testing. According to equation 2.12, the unknowns required to calculate the NRB include the received power and the overlap function since the transmitted power is directly monitored and the other variables are inherently provided through the lidar instrument. The overlap function can be set equal to 1 if the received light is entirely captured by the detector.

Calculation of Water-Vapor Absorption Cross Section

Three primary considerations were taken before arriving at the 828.187 nm water vapor absorption feature: the absorption-line strength had to be strong enough to attenuate the online wavelength by a sufficient amount, yet weak enough that the online signal could be measured beyond 6 km, the absorption cross-section needed as little influence by temperature changes as possible, and the absorption feature needed to be well isolated from other interfering absorption features. [24]

As a recap, by looking back to equation 2.3 we can see that the extinction due to absorption is defined by the absorption cross section, σ [cm^2], and the number density, N [molecule/ cm^3]. The absorption cross section can be separated into the molecular line intensity, S [cm/molecule], and the normalized line shape, g_ν [cm] as shown in equation 2.13. [33]

$$\sigma = S * g_\nu \tag{2.13}$$

The line intensity or line strength, S, is dependent on temperature and can be described as shown in equation 2.14 [24, 34, 35]

$$S(T) = S_0 \left(\frac{T_0}{T}\right)^{1.5} \left[\frac{1 - exp(-hc\nu_0/kT)}{1 - exp(-hc\nu_0/kT_0)}\right] exp\left[\frac{hc}{k}\left(\frac{1}{T_0} - \frac{1}{T}\right)E''\right] \tag{2.14}$$

where S_0 is the reference line strength for an absorption feature found at the center wavenumber , ν_0 [cm^{-1}], with a temperature, T_0 [K]. The chosen absorption feature will

have associated energy transition levels where E'' [cm^{-1}] is the lower of the two energy states involved in the absorbing process. These first four values can be found using HITRAN. [26, 35] The input, T [K], is the temperature of interest, and the remaining variables are all constants consisting of the Boltzmann constant, k, the speed of light, c, and Planck's constant, h. It has been found that an absorption feature with the minimal amount of dependence on temperature should have an E'' value ranging between 200 cm^{-1} and 300 cm^{-1}. [24, 36, 37]

The line shape, g_ν, is subject to natural broadening effects and shifting due to temperature and pressure changes. There are two primary sources of line broadening of the absorption feature through the atmosphere. These are Doppler broadening, which tends to dominate the line shape at low pressures, < 0.01 atm, and pressure broadening which tends to dominate the line shape at higher pressures, > 0.1 atm. [35]

The center of the absorption feature line will shift linearly with changes in pressure. The wavenumber of line center, ν_C [cm^{-1}], can be described in terms of pressure, P, as shown in equation 2.15, [35, 38] where ν_C^0 is the wavenumber of the line center at vacuum and δ is a linear rate of change parameter. These two parameters can be found using HITRAN. [26, 35]

$$\nu_C = \nu_C^0 + \delta P \tag{2.15}$$

Doppler broadening generates a Gaussian line shape which depends on atmospheric temperature. This dominates higher in the atmosphere above approximately 50 km and is a result of the variety of velocities and directions of the atoms and

molecules interacting with the light. The half- width at half-maximum (HWHM), γ_D [cm^{-1}], of this line shape can be described in terms of temperature, T, as shown in equation 2.16. [24, 35, 38]

$$\gamma_D = \nu_C \left(\frac{2kT}{mc^2}\right)^{1/2} \tag{2.16}$$

In this equation the wavenumber at line center, ν_C, as described above, must be known. The mass, m, in this case refers to the mass of the water vapor molecule.

Pressure broadening generates a Lorentzian line shape which depends on atmospheric pressure and temperature. This dominates lower in the atmosphere below approximately 2 km and results from collisions among the molecules that are interacting with the light. The Lorentzian HWHM, γ_L [cm^{-1}], of this line width can be described as shown in equation 2.17. [24, 35]

$$\gamma_L = \gamma_0 \left(\frac{P}{P_0}\right)\left(\frac{T_0}{T}\right)^{\alpha} \tag{2.17}$$

In this equation the HWHM, γ_0 , is defined at a standard pressure, P_0, and standard temperature, T_0, and α [unitless] is the linewidth temperature-dependence parameter. These four parameters can be found using the HITRAN database. [26, 35] The inputs for this equation then become the temperature and pressure of interest.

The Voigt distribution convolves both the Lorentzian profile due to pressure broadening and the Gaussian profile due to Doppler broadening, which helps to calculate

the final line shape by accounting for these two primary line broadening mechanisms found in the atmosphere. [38] The Voigt profile as a function of wavenumber can be described as shown in equation 2.18. [24, 35] This profile describes the line shape, g_ν, of the absorption feature.

$$V(\nu) = g_\nu = \frac{1}{\gamma_D\sqrt{\pi}}\frac{\gamma_L}{\gamma_D\pi}\int_{-\infty}^{\infty}\frac{e^{-t^2}}{\left(\frac{\gamma_L}{\gamma_D}\right)^2 + \left(\frac{\nu-\nu_C}{\gamma_D} - t\right)^2}dt \tag{2.18}$$

Using these equations and HITRAN to calculate the absorption cross section, the appropriate absorption feature was found by Nehrir et al. in the AORS laboratory at MSU. [24] The chosen absorption feature has a line center (online) wavelength at 828.187 nm in vacuum and an offline wavelength at 828.287 nm in vacuum. In order to accommodate for changes in atmospheric conditions throughout the year, the absorbing wavelength can be tuned along the side of the absorption feature between 828.19 nm and 828.195 nm in vacuum. The line parameters for the chosen absorption feature include a ground state transitional energy of E''=212.2 cm^{-1}, a line strength of S=1.477x10^{-23} cm^{-1}/(molecule cm^{-2}), a standard pressure broadened linewidth (FWHM) of γ_0=0.1937 cm^{-1} at 1 atm and 273.15 K, and a linewidth temperature dependence of α=0.68. [24]

WATER VAPOR DIAL INSTRUMENT

Transmitter

A schematic of the laser transmitter is shown in figure 3.1. The laser transmitter utilizes two distributed Bragg reflector (DBR) diode lasers. The diodes are set in a TO-8 package and

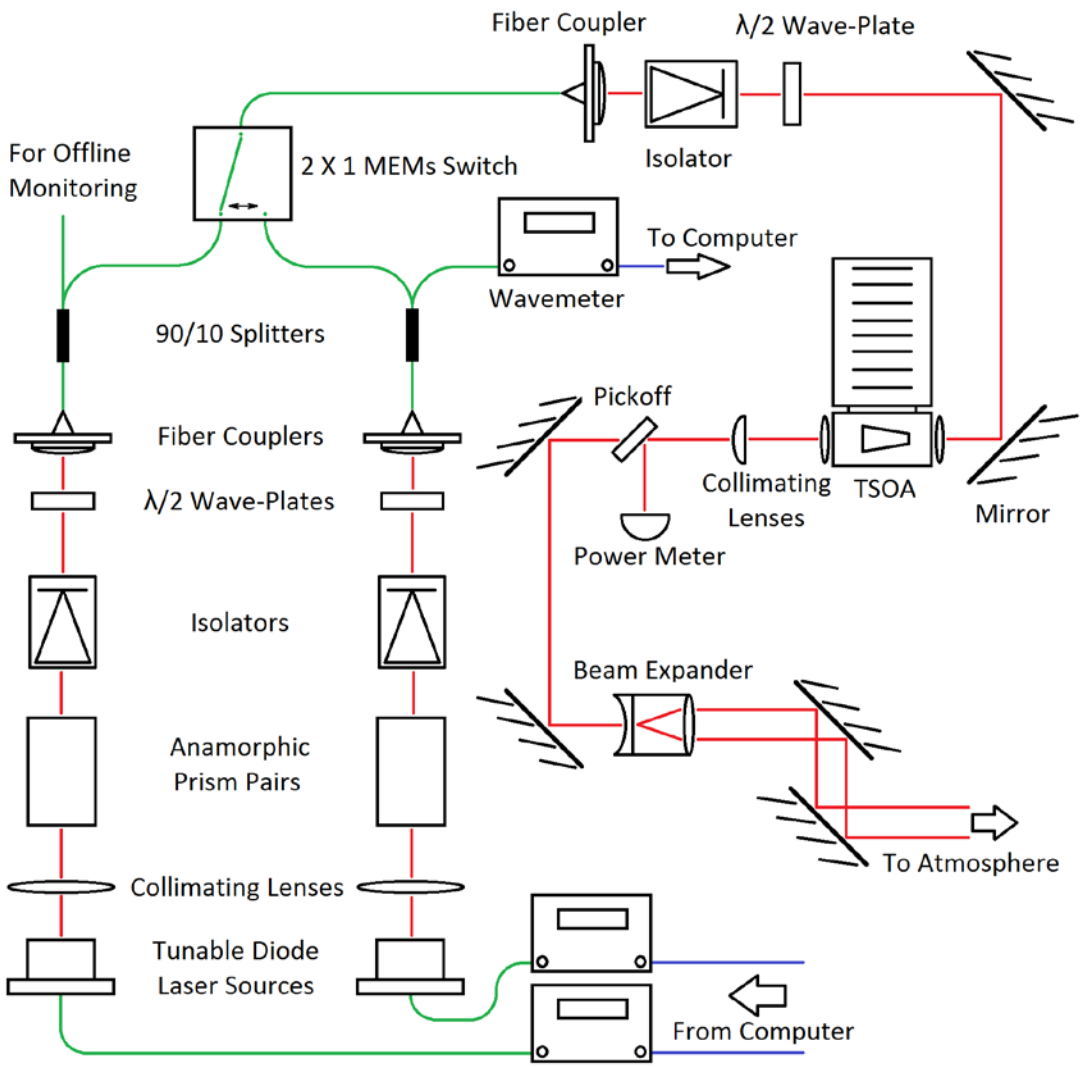

Figure 3.1: Schematic diagram of the DIAL laser transmitter.

purchased from Photodigm. (Part number PH828DBR100T8) The beam is nominally collimated and reshaped using an aspheric lens and an anamorphic prism pair respectively. The aspheric lens has a focal length of 4mm and a numerical aperture of 0.6. The anamorphic prism pair is from Thorlabs and has 4.0x magnification. (Part number PS883-B) These steps ensure that the beam will remain small enough to be fully fiber coupled. The light is then sent through a Faraday isolator and a half wave plate from Thorlabs. (Part numbers IO-3D-830-VLP and WPH05M-830 respectively) The isolator is used as a protective measure to prevent both wavelength instability due to back reflections, as well as more intense back reflections that can cause physical damage to the diodes. The half-wave plate is used to align the linear polarization from each laser with the polarization maintaining (PM) fiber that the light is then coupled into. The fiber couplers used were purchased from Thorlabs. (Part number PAF-X-11-B) With proper polarization and beam size, approximately 50% of the optical power is coupled into the PM fiber. All fibers used in this experiment are angled physical contact (APC) to reduce back reflections in the system.

The first fiber leads to a 90/10 fiber optic beam splitter, and was purchased from Newport. (Part number F-PMC-850-10) Ten percent of the coupled beams are used to monitor the wavelength with an optical wavemeter. The wavemeter was manufactured by EXFO. (Part number WA-1500) The online laser is stabilized using the wavemeter for feedback. The wavelength information is passed on to the computer which will make slight adjustments to the driving current of the online DBR laser. The two lasers are controlled by temperature and driving current using diode controllers purchased from

ILX Lightwave. (Part number LDC-3724B) If the online laser drifts at all, the computer sends adjustment commands to the diode controllers to correct the drift. The offline (outside absorption wavelength range) laser is adjusted and set before data collection starts using the available 10 percent splitter output. During data collection, this port is not monitored continuously since the amount of drift observed by the laser is much less than the amount of detuning required for absorption effects to alter the measurement. During autonomous operation, the online wavelength is continuously directed to and monitored by the wavemeter.

The remaining 90% from each laser is fiber coupled into a mechanical fiber optic switch that allows either the online laser or the offline laser through the system. The switch was made by Agiltron. (Part number LBPM-128238333) The switch is controlled by the computer and switches approximately every three seconds between wavelengths. The switch output re-collimates the light with another fiber coupler from Thorlabs with a focus of 4.6mm and an N/A of 0.53. (Part number PAF-X-5-B) A Faraday isolator is then used to control back reflections to and from the amplifier from returning back through the system, which has been observed to cause wavelength destabilization. This isolator is the same as the two protecting the laser diodes. A half wave plate is then used to set the orientation of the linear polarization to peak the coupling into the amplifier. (Part number WPH05M-830 from Thorlabs)

The light is then used to injection seed a tapered semiconductor optical amplifier (TSOA) made by Eagleyard. (Part number EYP-TPA-830-01000-4006-CM-T04) The amplifier gain region is a 4mm long ridge waveguide and is controlled with a temperature

controller and a current controller. The temperature controller maintains a constant temperature during operation, while the current controller sets the gain and divides the light into pulses. The temperature controller used came from ILX Lightwave. (Part number LCT-5525B) The current controller came from DEI Scientific. (Part number PCX-7420) The current controller is capable of producing up to 15.7 A pulses with a frequency of 1 MHz and a pulse duration of 5 ms. [32] The rise and fall time for each current pulse is 25 ns. During actual operation, the amplifier is set to 10 A with a 1 µs pulse duration and a frequency of 10 kHz, providing 10.3 µJ pulses or a saturated average output power of approximately 100 mW. The optical power seeded into the TSOA was measured to be 12.6mW for the online wavelength and 13.9mW for the offline wavelength. These seed powers are high enough to fully saturate the amplifier, meaning slight fluctuations from the diodes will not affect the output energy of the transmitter. The TSOA emits the light with a vertical (perpendicular to the bench top) divergence angle of 28° and a horizontal divergence angle of 15°. In order to re-collimate the beam out of the amplifier, a two-step process has been implemented. A spherical collimating lens with a focal length of 4.5 mm is first used to collimate the vertical diverging beam. This also overcorrects the horizontal spread, bringing it back to a focus in the horizontal direction. It is then fully collimated using a cylindrical lens with a focal length of 50 mm.

With the beam nominally collimated, a pickoff is used to redirect approximately 2% of the light onto a power meter detector to monitor the output power of the system. The power meter and the detector head were purchased from Newport. (Part numbers 1918-R and 918D-SL-OD3 respectively)

The beam is then sent through a 5x beam expander from Thorlabs. (Part number BEO5M) This is used to both spread the beam to decrease the divergence angle through the atmosphere, and to spread the optical power over a larger area to help meet eye safety requirements. The outgoing beam is approximately 3 cm in diameter. The beam is sent through a two mirror periscope to align with the optical axis of the telescope on the receiving optics side of the system.

The two lasers produce up to 80mW of continuous wave (cw) optical power and can be wavelength tuned with the temperature and the driving current. The wavelength is tuned by temperature at a rate of 0.059 nm/°C and a driving current rate of 0.0011 nm/mA. The measured FWHM linewidth for both lasers is 0.023 pm (1 MHz). The online laser (within absorption wavelength range) is monitored with an optical wavemeter. The accuracy of the wavemeter measurement is ±0.125 pm, which sets the uncertainty in the operating wavelength. Since the laser linewidth is approximately 100x smaller than the absorption feature linewidth, the online laser can be tuned up or down the side of the absorption feature, allowing for more or less total absorption of the return scattered light. Setting the amount of absorption is important since the atmospheric conditions can be highly variable throughout the year, and the peak performance of the instrument is dependent on the chosen amount of absorption. [24] Too much absorption will decrease the distance of the water vapor measurement through the atmosphere. Too little absorption will lead to incorrect water vapor measurements. The absorption cross section is set such that the optical depth at the desired maximum altitude is approximately 1 to 2. [32]

Receiver

A schematic of the DIAL receiver is shown in figure 3.2. A Celestron 14" Schmidt-Cassegrain telescope is used to collect the back-scattered light. It has a focal length of 3910mm and an F/# of 11. Behind the telescope an adaptor is used to connect the remaining receiver via light tight tube assembly. A field lens with a focal length of 7.5 cm and a diameter of 2.54 cm is placed at the focus of the telescope to help correct for the outer, extreme rays propagating through the system while allowing the more central rays to pass almost unhindered. A collimating lens is then placed 5 cm after the focus of the telescope. This lens has a focal length of 5 cm and a diameter of 2.54 cm. The collimated light was sent through two narrowband optical interference filters, which provided enough noise extinction to allow for clear daytime measurements. The filters have linewidths of 500pm and 750pm, and are both centered at 828.007nm and achieve peak transmissions of 70%. These filters were purchased from Alluxa and Materion respectively. After filtering, a fiber coupler lens with a focal length of 1.1 cm and a clear aperture of 4.4 mm was connected to a step index optical fiber with a core diameter of 105 µm and a numerical aperture of 0.22. The fiber acted as the field stop for the far-field receiver system, setting the full angle field of view to 224 µrad. A fiber coupled Avalanche Photo Diode (APD) was used as the detector to count returned photons. Since only around 10 counts could be expected per pulse, the data was then sent to a multichannel scalar card (MCSC) which placed the counts in time bins that sync with the laser pulse. The MCSC adds up the data from 10,000 pulses before sending the data to

the computer. This ensured that the return signal would be distinguishable from background noise.

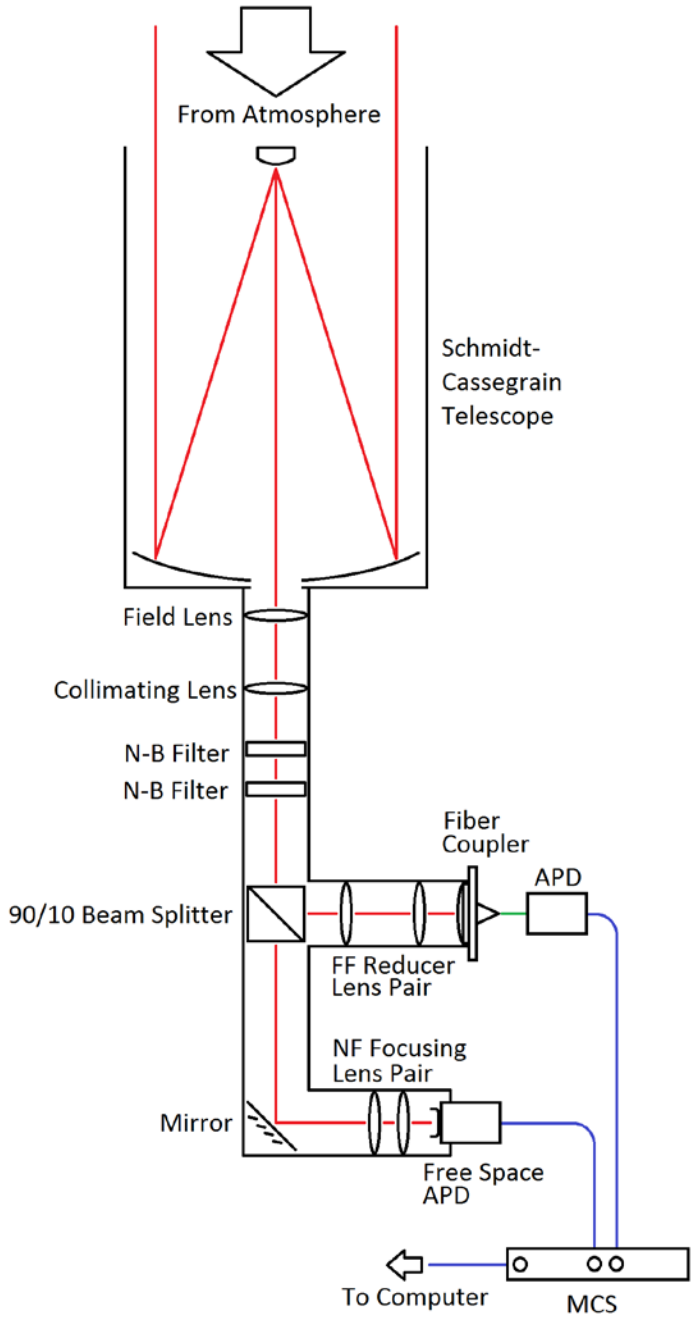

Figure 3.2: Schematic diagram of the DIAL receiver.

The return signal between 500 m and 2 km can now be measured in full overlap by the system with a separate near-field detection channel. A 90/10 beam splitter was added after filtration to send 10% of the return signal to a second APD. The optical train following the beam splitter focuses the light returning from the near-field range onto the detector. With the current setup, all the captured light returning from between 500m and 5km is captured by the detector. The additional detection channel implemented a free space APD with a larger detection surface, effectively opening up the field of view now set by the telescope focus to 970 µrad.

Ray Tracing Model of the Two Channel Receiver

A new optics train had to be designed to bring the return scattered light from below 2km into full overlap of the detector. A first order design was laid out using ABCD matrices. [32] This method is a ray analysis technique used to keep track of the ray's distance, R, from the central optical axis as well as its angle relative to the optical axis, R'. These variables can be kept track of using the vector $R = \begin{pmatrix} R \\ R' \end{pmatrix}$.

For the first order modeling of this system, only the lenses and free space propagation need to be considered. These can be modeled using the matrices $M_l = \begin{pmatrix} 1 & 0 \\ -1/f & 1 \end{pmatrix}$ and $M_{fs} = \begin{pmatrix} 1 & d \\ 0 & 1 \end{pmatrix}$, where M_l models a lens of focal length f, and M_{fs} models a propagation of distance d. With all lenses and distances defined, the entire optical system can be characterized by one 2x2 matrix, $M = M_n M_{n-1} \ldots M_2 M_1$ where the subscript values represent the order in which the optical element is encountered by a propagating ray. The output ray, R_O, is defined by $R_O = MR_I$, where R_I is the input ray.

Figure 3.3 shows a diagram of how the near field optical layout is represented by matrices using this model. The matrices must be in sequence; M_1 represents the telescope on the far left and the subscripts continue in order through M_9 on the far right. Each optic is represented as a lens matrix and each propagated distance is represented with a distance matrix. It can be noted that the near field focusing lens pair was calculated using zero distance between them. When combining these matrices as described above, the output position and angle will be at the location of the detector for a given input ray position and angle. The far field was calculated in the same manner.

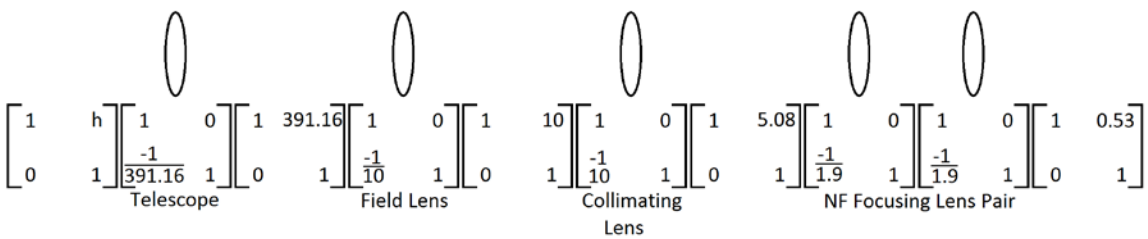

Figure 3.3: Layout of the optical model for the near field receiver using ABCD matrices showing M_1 through M_9 from left to right. The value "h" represents the distance from the reflecting particle to the telescope and was scanned from 0 to 12 kilometers.

A transmitted beam model was created assuming an initial beam radius of 2 cm and a full angle beam divergence of 25 μrad. This model is used to find the object diameter to be used as the input to the system model, R_I. The image diameter at the focus of the optical receiver system could then be calculated using the above described receiver model. The fiber acts as the field stop of the far field system, providing both a maximum diameter allowed for full overlap of the beam returning from any given altitude, 52.5 μm, as well as a maximum ray angle allowed into the fiber, 0.22 rad. In order to change the altitude at which full overlap is achieved, the fiber end can be adjusted away from the

focus of the final lens in the system by an offset amount. Figure 3.4 shows a scan of the beam radius at the fiber input versus beam altitude. The various colors in the plot show offsets of the fiber away from the focus of the final lens, demonstrating how full overlap can be achieved through the use of this adjustment. The radius of the fiber is provided with the vertical black line, and serves as a reference in choosing the best final position of the fiber in the system. The offset for this system was set to approximately 200 μm to allow full overlap to begin at 2.1 km, and continue up to 12 km.

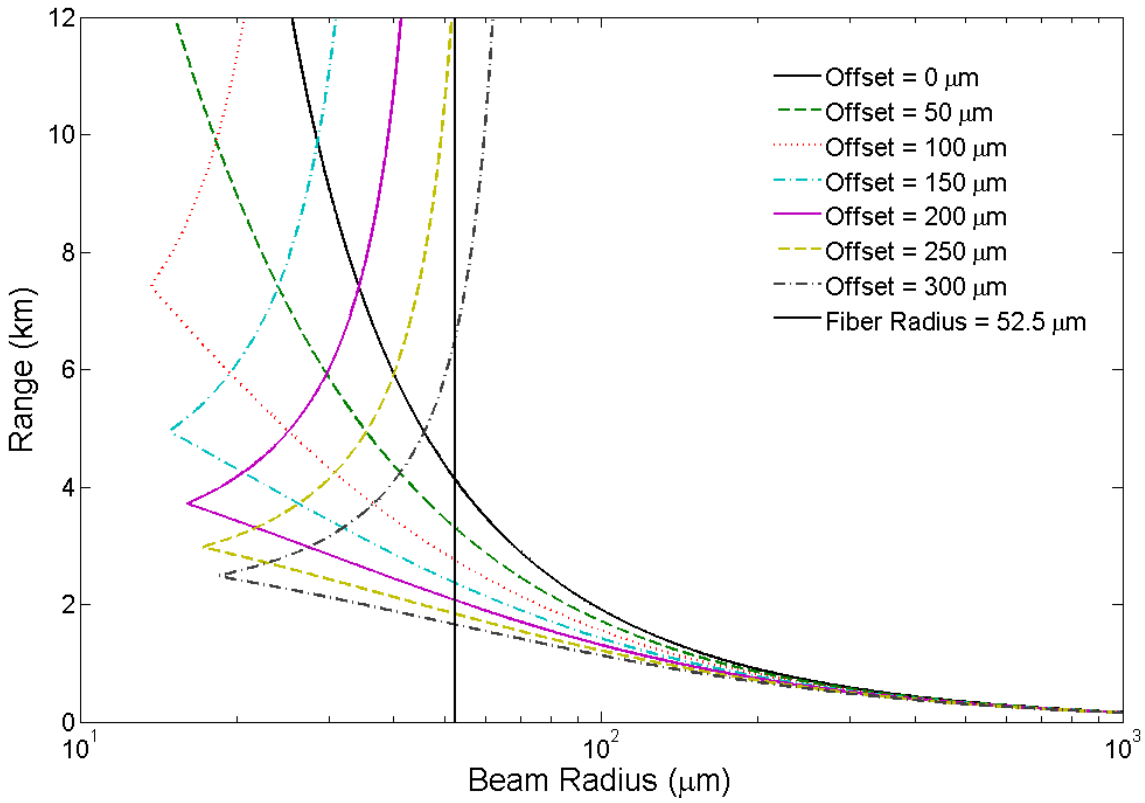

Figure 3.4: Plot of beam radius at the fiber input versus beam altitude for various offset distances between the fiber input and the focus of the fiber coupling lens.

The maximum beam angle seen at the entrance of the fiber was found by running four beams representing the most extreme starting positions and angles that could still be

captured by the telescope. The most extreme beams were found to come from one edge of the object and land either on the same edge of the telescope or on the opposite edge of the telescope. The angle of the most extreme rays needed to be checked in order to verify that all the captured light would fall within the maximum allowable beam angle of the fiber. Figure 3.5 shows the maximum beam angle seen at the fiber versus beam altitude. The allowable angles into the fiber peak at +/- 0.22 radians. Using the model from above, the maximum ray angle is satisfied above 400 meters and up beyond 12 km.

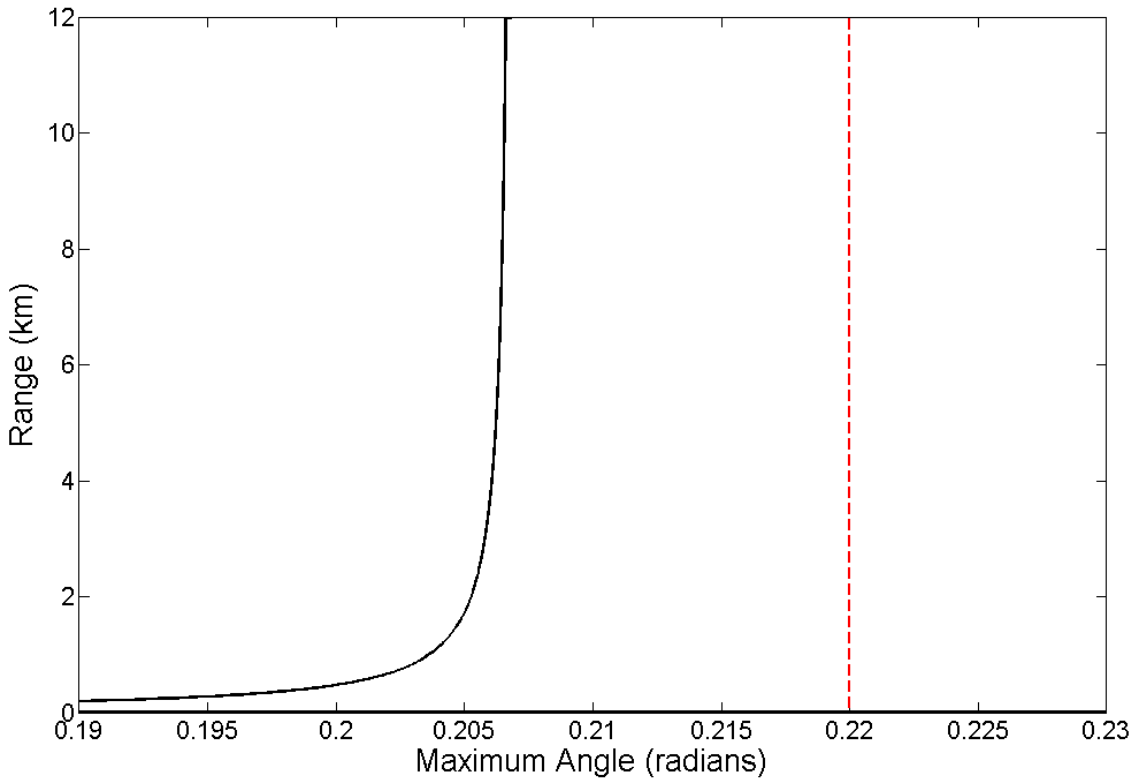

Figure 3.5: Plot of maximum beam angle seen at the fiber versus beam altitude with maximum allowable beam angle shown by the red dashed line.

The near field channel uses a free space detector at the end of the near field optics train. This means the acceptance angle will be limited by the remaining optical elements

in the system, rather than the detector. Based on the diameter of the free space detector, 90 μm, and using the above described model for the near field optics, the position of the near field detector can be found for an optimal overlap. Figure 3.6 shows the beam diameter that is achievable for various offsets in detector placement.

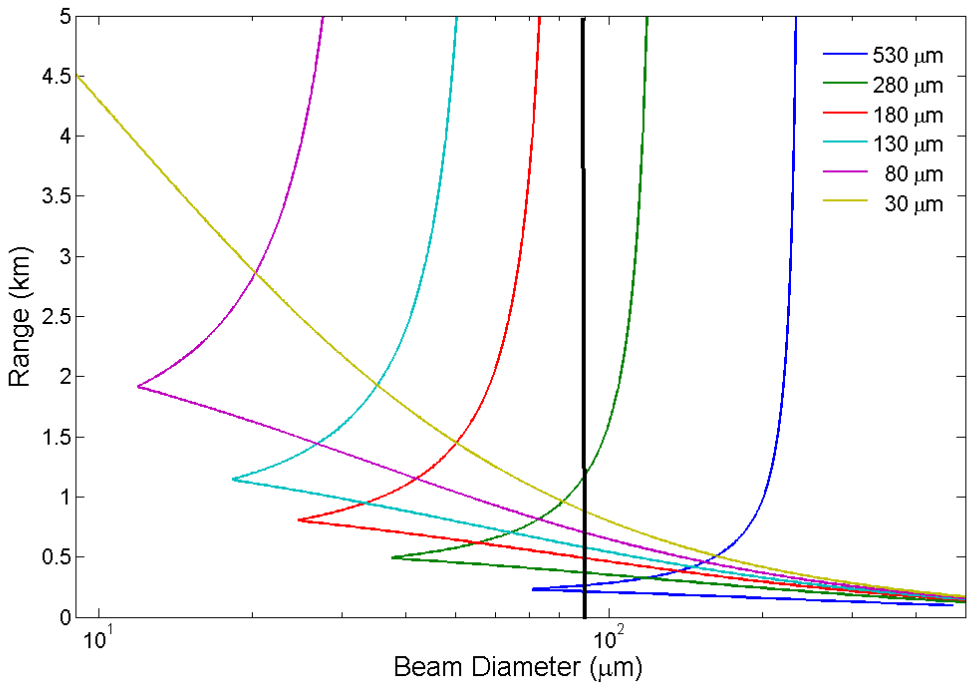

Figure 3.6: Plot of beam radius at the near field detector input versus beam altitude for various offset distances between the detector and the focus of the detector focusing lens.

Zemax Model of the Two Channel Receiver

The receiver was modeled using Zemax [32] (commercial optical design software) as a ray tracing model to show proof of concept behind the re-design of the receiver and to verify the accuracy of the ABCD matrix model, effectively establishing a simple method of analyzing and designing the receiver optical train. The model was built up using all the appropriate Thorlabs lenses which can be found in the Zemax lens

catalog. The Schmidt-Cassegrain telescope, however, needed to be built from scratch as the Zemax model was not available for public use. The telescope was designed with a focal length of 391.2cm and a primary mirror diameter of 35.6cm.

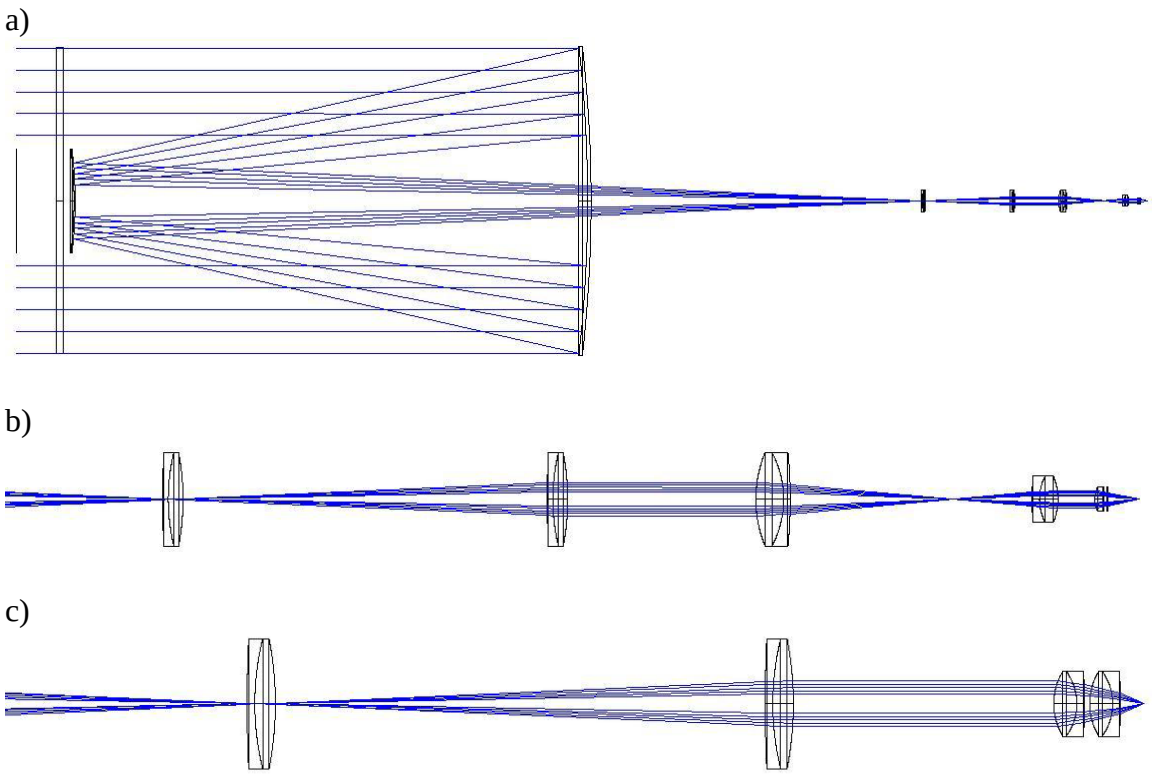

Figure 3.7: Zemax lens diagram model for a) telescope, b) far field channel, and c) near field channel.

Figure 3.7 shows the receiver model with purely collimated light at the input. More specifically, figure 3.7 a) shows the entire far field channel, figure 3.7 b) shows a blown up view of the far field optical train following the telescope, and figure 3.7 c) shows a blown up view of the near field optical train following the telescope.

The data set from the Zemax model was compared to the ABCD matrices model. Figure 3.8 shows the radius of the beam after the telescope and re-collimating lens pair as

a function of range. Recorded data points from Zemax are shown with green circles, while the ray tracing model is depicted with a blue line. A small shift down in beam radius is observed from the Zemax model with deviations of 0.70%, 0.53%, and 0.02% at 0.5 km, 1.0 km, and 12 km respectively.

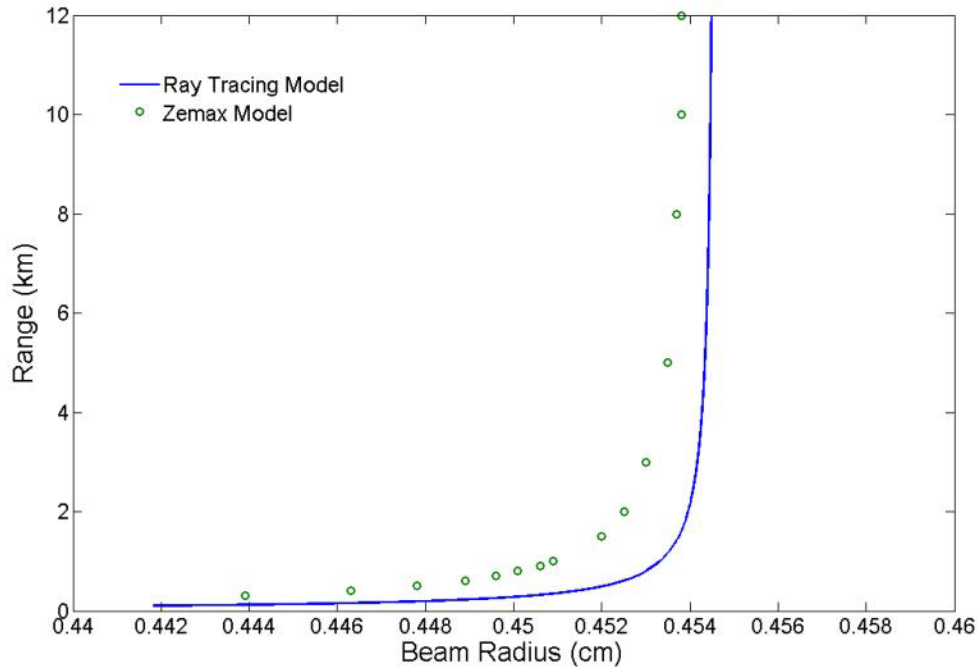

Figure 3.8: Comparison of ray tracing model to Zemax model of beam radius vs range measured after collimation of the light through the telescope.

This is most likely due to the Zemax model considering the thickness of each optical element, as well as aberrations that will affect the structure of the beam. Knowing the radius of the beam through the 1.27 cm radius filters and remaining receiver optics is important to plot as a quick verification making sure that no clipping along the edges of the receiver will occur. Figure 3.9 shows the maximum ray angle after the same collimating lens as a function of range. This is another important consideration as the two filters have some angle dependence and operate best with collimated light. Noting this is

the maximum angle traveling through the filters and the majority of the back reflected light will be closer to collimated, we still see low deviations less than 0.01 radians down

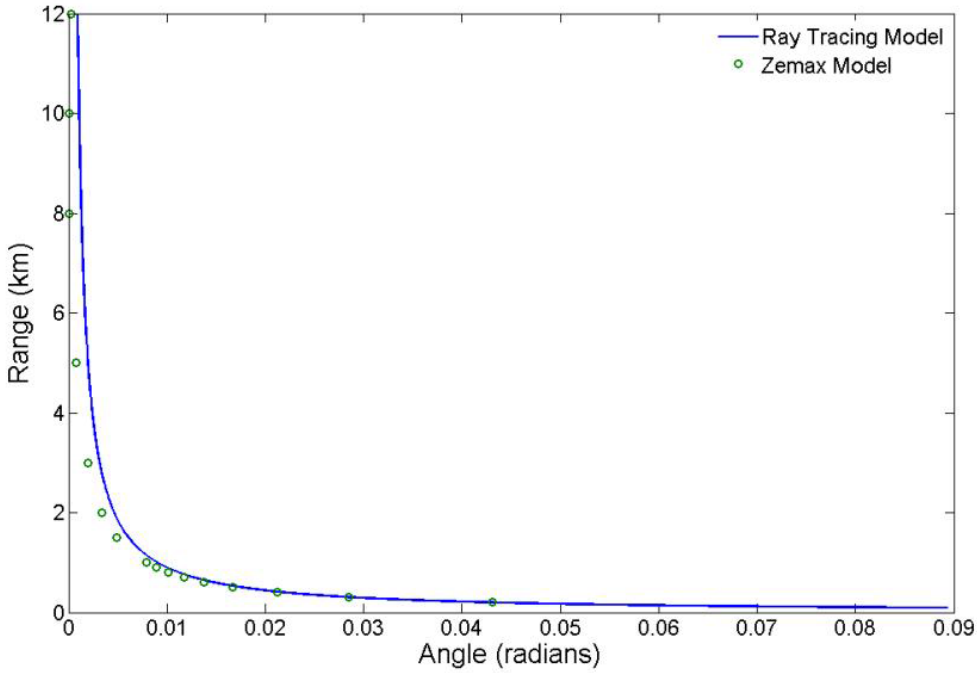

Figure 3.9: Comparison of ray tracing model to Zemax model of maximum ray angle vs range measured after collimation of the light through the telescope.

to 700 m. These angles will have a negligible effect through the filters. Again, the two models are in close agreement, with a deviation of 7.8% at 0.5 km.

Continuing on through the receiver, the Zemax model can be used to check the beam diameter and the maximum ray angle into the fiber leading into the far field detector as well as the beam diameter at the near field detector. Figure 3.10 shows the Zemax and ray tracing models at the far field fiber entrance. The solid lines and circles once again represent the ray tracing model and Zemax model respectively. The blue colored data represents the fiber placement at the focus of the final lens and the green

colored data represents the fiber placement at 150 μm behind the focus of the final lens. The vertical black line represents the radius of the optical fiber. This plot is critical in

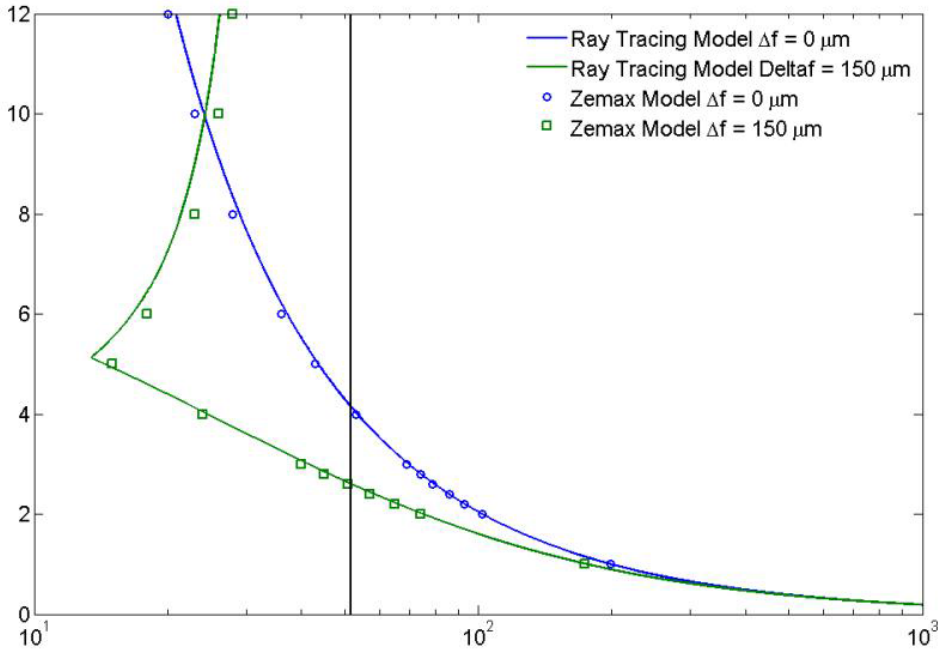

Figure 3.10: Comparison of ray tracing model to Zemax model of beam diameter vs range measured at the location of the fiber.

showing with certainty where the theoretical overlap of the receiver will occur. As long as the radius of the beam is less than the radius of the fiber, full overlap is possible since no clipping will occur. Optical fibers also have entrance angle dependence which must be considered before knowing where full overlap is actually achieved. The deviation between the two models for the blue configuration is 1.7% and 4.4% at 5 km and 12 km respectively. The green configuration shows similar agreement between the two modeling methods with both suggesting full overlap begins at 2.3 km.

Figure 3.11 shows the maximum ray angle at the fiber. The maximum acceptable ray angle of the fiber in this system is 0.22 radians. Again, the Zemax modeling is in close agreement with a deviation of 0.6% at 12 km. Both models indicate that the peak

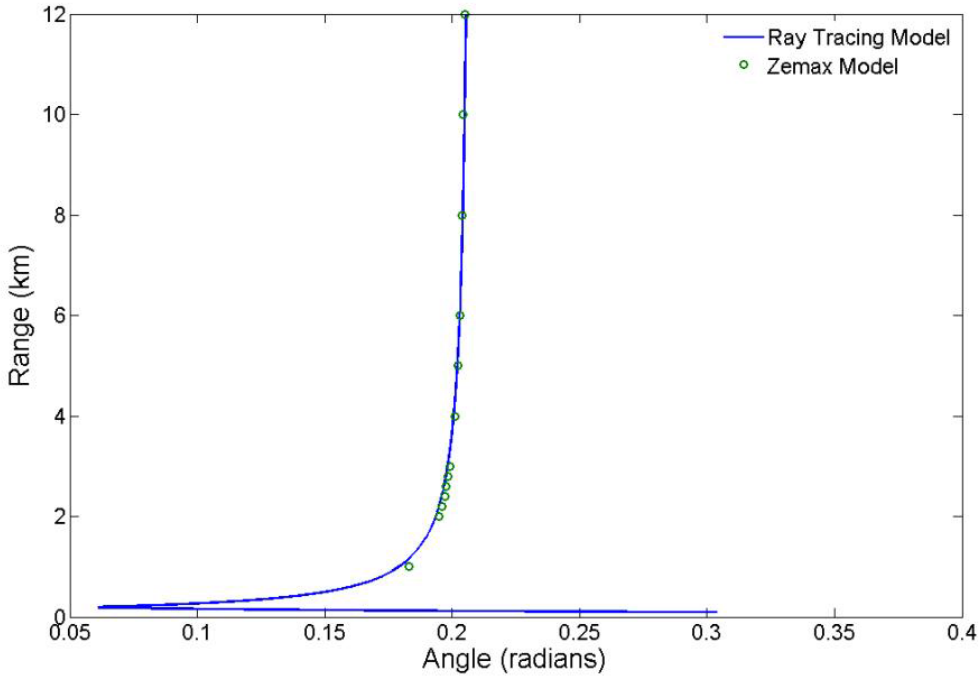

Figure 3.11: Comparison of ray tracing model to Zemax model of maximum ray angle vs range measured at the location of the fiber.

angle into the fiber remains smaller than its accepted 0.22 radians between 0.2 and 12 km. This tells us that the far field channel is capable of achieving full overlap starting at 2.3 km where clipping of the beam diameter begins to take hold at lower altitudes as shown by figure 3.10.

Figure 3.12 shows the two models at the near field detector. The blue colored data represent the detector placement at the focus of the final lens in the near field optics train and the green colored data represents the detector placement at 180 μm behind the focus

of the final lens. The vertical black line represents the radius of the free space detector. Since the near field channel utilizes a free space detector, the incidence angle at the detector doesn't matter and the attitude at which full overlap occurs can be seen directly

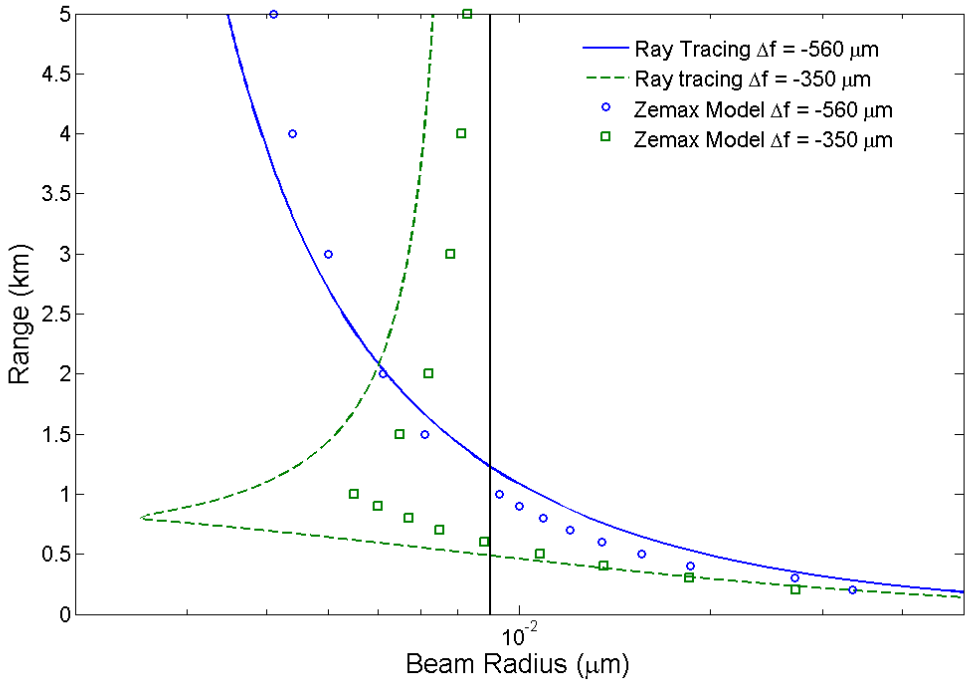

Figure 3.12: Comparison of ray tracing model to Zemax model of beam radius vs range measured at the near field detector.

from this beam radius plot. The deviation between the two models for the blue configuration is 16.5% and 28% at 1 km and 5 km respectively. The green configuration again shows similar agreement between the two modeling methods with both showing full overlap occurring at and above 0.6 km.

After using Zemax software to validate the linear ABCD matrices model, it can be seen that the ray tracing method is entirely qualified to model any future changes to the receiver system. It is an easy model to implement in MATLAB computational software

and can be easily modified, providing the designer with good understanding and intuition in how minor adjustments can affect the performance of the overall receiver.

Programming for Autonomous Deployment

In order to get the desired water vapor measurement, two LabVIEW programs were used. The first program simply communicated directly with the scalar card. This program provided the settings to the scalar card such as how many range bins to divide

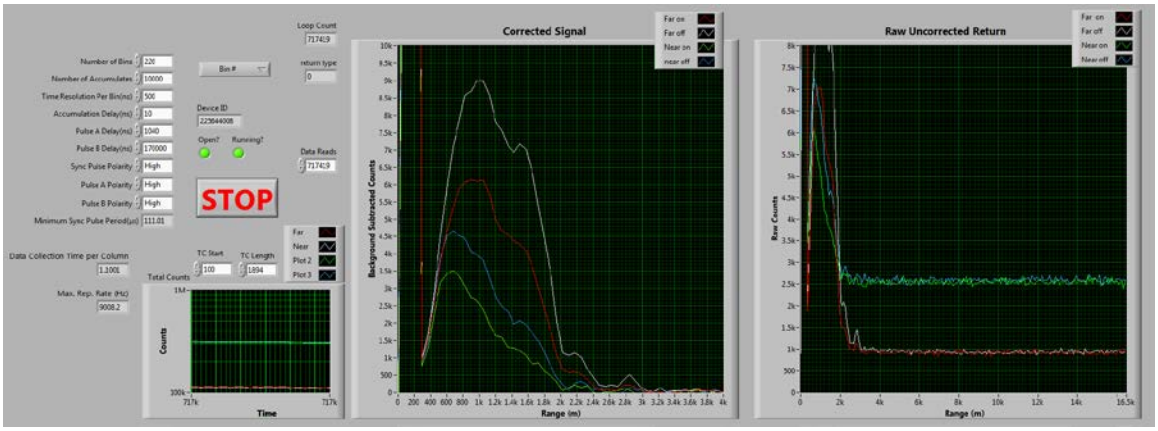

Figure 3.13: Screen shot of the user interface for the scalar card program which shows a live feed of the raw data return.

the data into and how many iterations of retrieval to require before sending a packet of data to the computer. This program also read and plotted the raw data for the user. This program was important in achieving proper alignment of the receiver. The user interface of this program is shown by figure 3.13.

The second program was used to control the remaining equipment and collect data autonomously. The user interface of this program is shown in figure 3.14. This program required communications with the current adjustment on the two laser diode controllers,

the wavemeter, the power meter, and the switch used to separate the online and offline wavelengths. It also called on the data from the scalar card program and used that data to calculate the normalized relative backscatter and the water vapor. The primary function of this program is to adjust the wavelength of each diode as necessary, to set the switch to

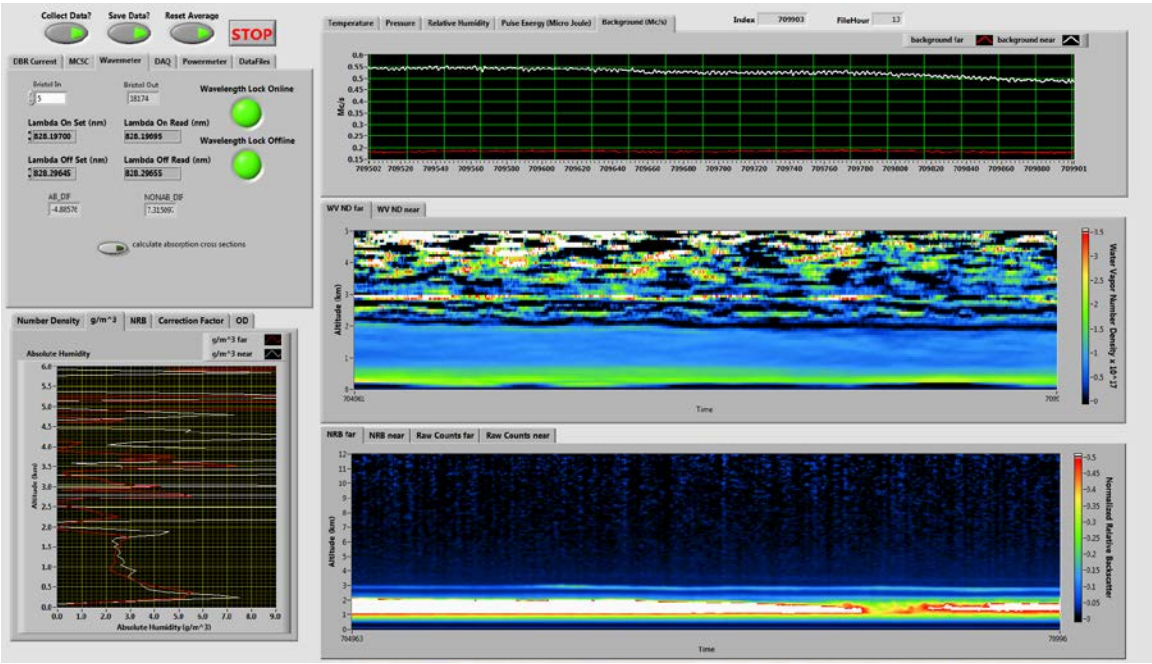

Figure 3.14: Screen shot of the user interface used to set the wavelength while observing a live feed of measurements such as water vapor and NRB.

pass the appropriate wavelength, to provide a live feed of the water vapor, NRB, and other information of interest, and to archive the data to the computer.

The wavelength of both lasers was controlled by first reading the wavelength of the laser with the wavemeter. The desired wavelength can be programmed into the LabVIEW interface and was set to a tolerance of +/- 0.2 pm, which automatically corrects for insignificant, natural wavelength fluctuations that occur without impacting the data collection. The wavelength reading is then compared with the desired wavelength and

adjusted if needed using the appropriate laser diode current controller adjustment. After each 0.01 mA step in diode current towards the desired wavelength, a new reading is taken from the wavemeter. This process occurs until the individual diode is within the set tolerance.

EXPERIMENTAL RESULTS

Data Collection Summary

The water vapor DIAL instrument collected data continuously and autonomously over a ten day period from July 17, 2013 until July 27, 2013 at Montana State University. This data run was conducted in a laboratory environment. The transmitted and received beams travel through a roof port window which protected the DIAL from outside weather systems such as rain, wind, and large temperature fluctuations. The roof port window is not antireflection coated for 830 nm and results in a 20% loss in signal after the double pass. Over the period of this data run, stormy conditions occurred from July 17th to July 18th and from July 26th to July 27th. The days in between, July 19th through the 25th, were all clear or partly cloudy. This data run was conducted upon achieving proper alignment of the far field channel only and was verified through comparison with multiple radio sonde launches. A second data run was conducted under the same conditions over 71 days from August 1st, 2015 until October 10th, 2015. This data set included a wide variety of weather conditions and showed the ability to take continuous and autonomous water vapor measurement. The near field channel was properly aligned throughout this data run. Using some of the clear days, a comparison between the far field and the near field channel was conducted, and provided results suggesting 1) that the near field channel indeed had a lower full overlap and 2) both channels produced similar water vapor number density measurements.

Far Field Verification

The two main data products produced by the DIAL system include the normalized relative backscatter and the water vapor number density. Normalized relative backscatter provides a range corrected profile of aerosol density and distribution information and is calculated from the transmitted power, a geometric model of the range dependent overlap, and the return power for a given distance. The overlap function is needed particularly for the data received by the far field channel below 2.1 km since the light captured by the telescope from that region doesn't couple entirely onto the detector.

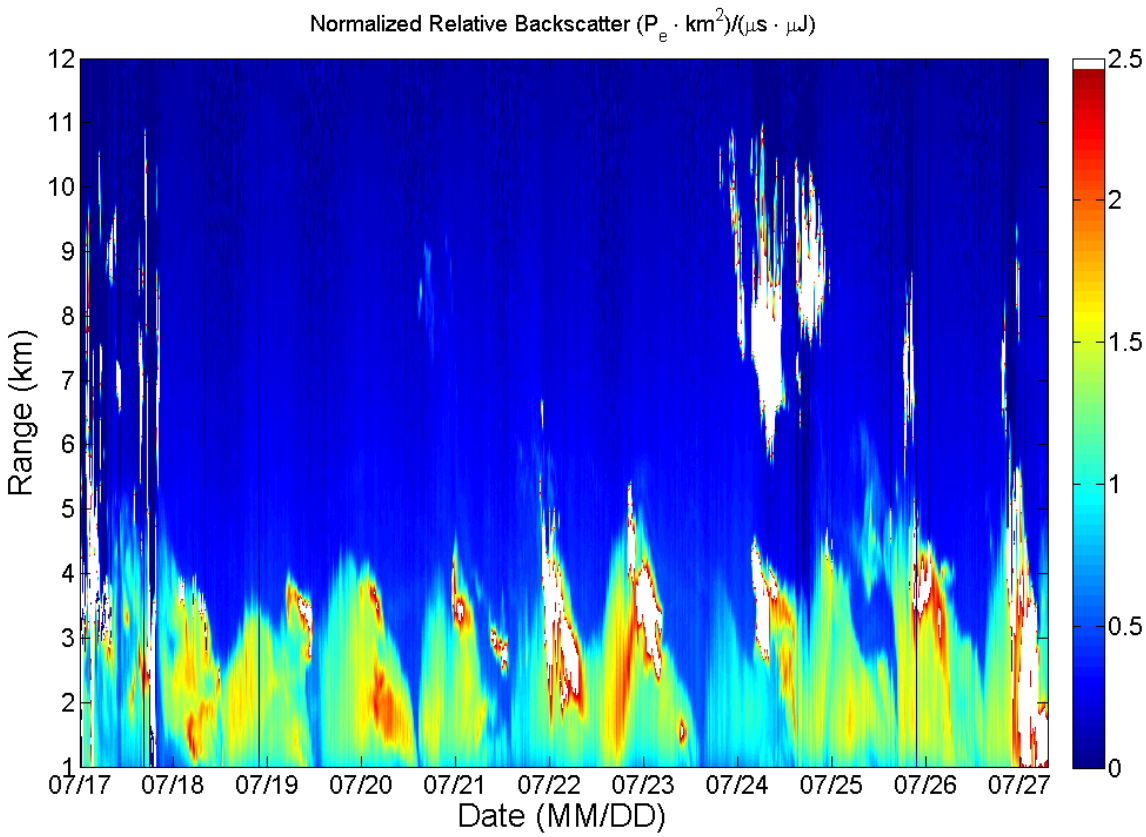

Figure 4.1: A plot of the measured normalized relative backscatter ranging from July 17th 2013 through July 27th 2013.

Water vapor number density provides a profile of the absolute density of water vapor in the atmosphere vs altitude and is calculated using the return power for a given distance, the difference in absorption cross section between the two wavelengths, and the filter efficiency for each wavelength and relative angle. Figure 4.1 shows a plot of relative backscatter from the far field channel over the entire collection period of the first data run in July 2013. Figure 4.2 shows a plot of the water vapor number density from the far field channel over the same collection period.

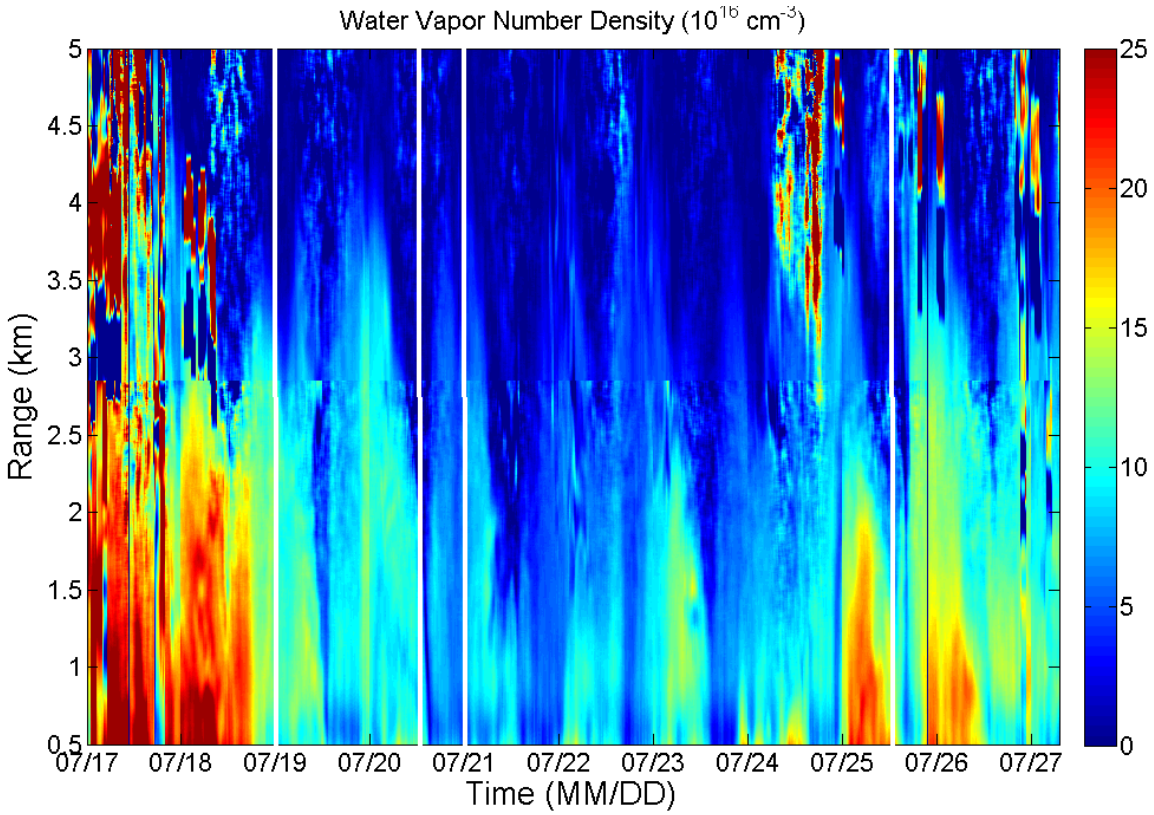

Figure 4.2: A plot of the measured water vapor number density ranging from July 17th 2013 through July 27th 2013.

The water vapor number density measurement was checked against radio sonde measurements. Balloons were launched on July 19th at 12:16am MDT, July 20th at 12:45pm MDT, July 20th at 9:55pm MDT, and on July 25th at 11:21am MDT. A profile of the measured water vapor taken during each of these flights is shown in comparison to the sonde measurements in Figure 4.3. These comparisons were taken at different times of the day and under different weather conditions. These plots show good agreement, averaging approximately 2 percent error among all four cases between the DIAL measurement and the radio sonde measurement.

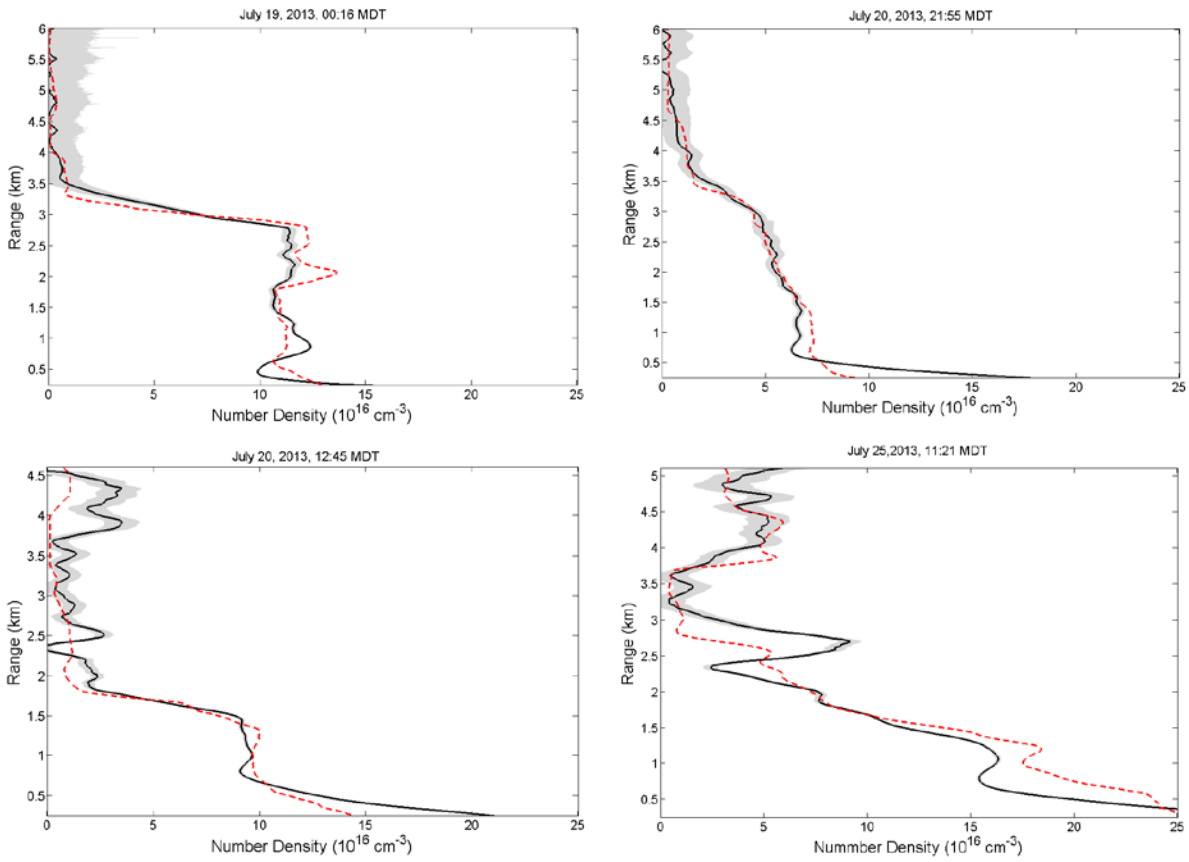

Figure 4.3: Four plots showing measured water vapor number density profiles in solid black compared to radiosonde data in dotted red at four different times during the data run in July 2013.

Near Field Verification

Knowing that the far field channel was fully functional, the near field channel was then added to the instrument as described in chapter 3. After much work, a complete data run with a functional near field channel was started in August of 2015 and spanning 71 days. The complete autonomous data set is shown in the following eight figures. (figures 4.4 through 4.11) Figures 4.4 through 4.7 refer to the far field channel and show the offline background counts/sec, the column optical depth at 2500m (blue) and 5000m (red), the relative backscatter, and the water vapor number density over the entire data run sample. Figures 4.8 through 4.11 show the same four plots, except for the near field channel.

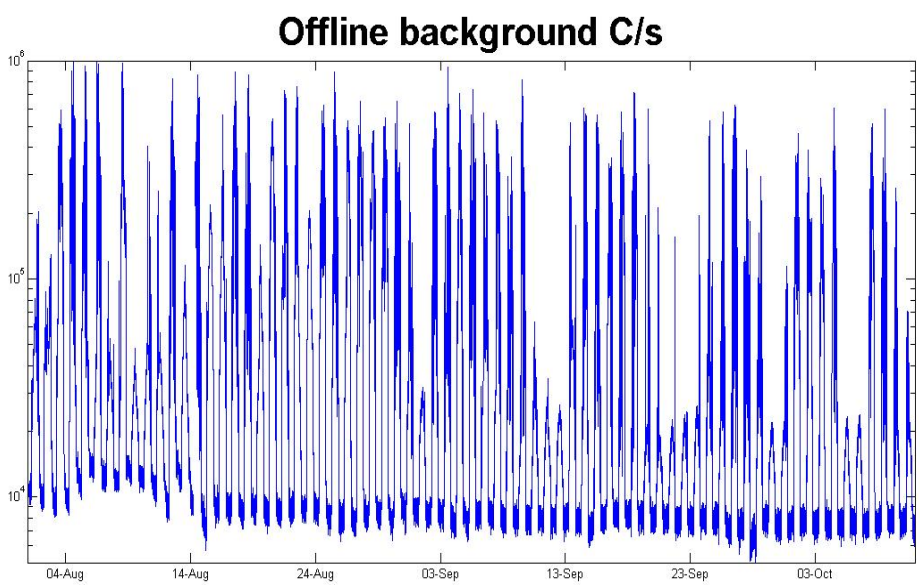

Figure 4.4: A plot of the measured offline background counts per second from the far field channel ranging from August 1st 2015 to October 10th 2015.

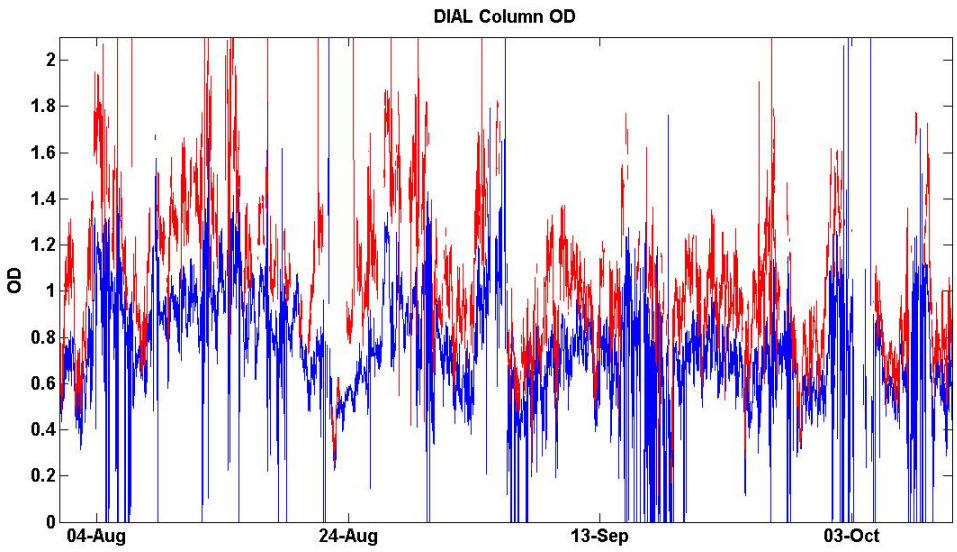

Figure 4.5: A plot of the column optical depth from the far field channel ranging from August 1st 2015 to October 10th 2015.

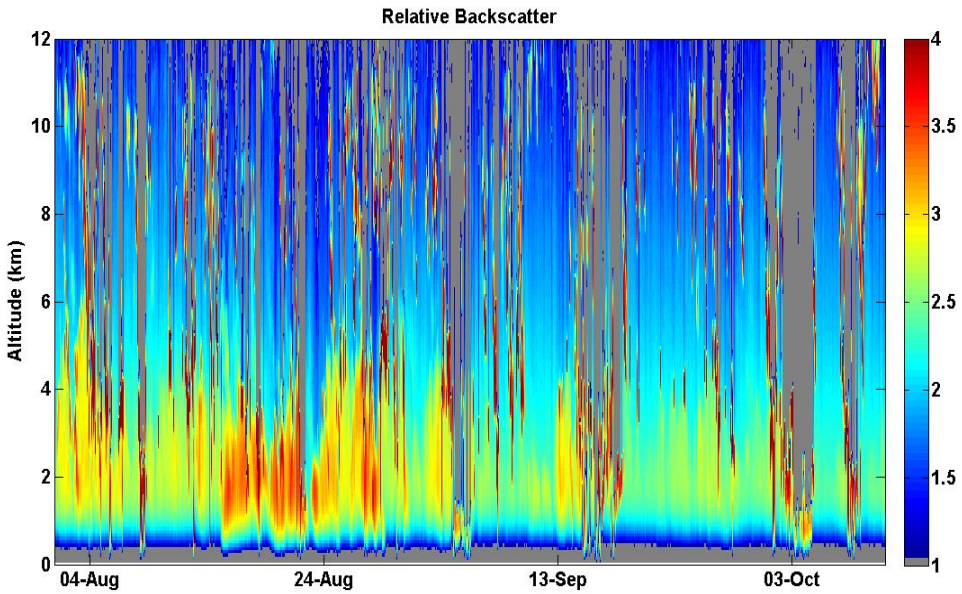

Figure 4.6: A plot of the relative backscatter from the far field channel ranging from August 1st 2015 to October 10th 2015.

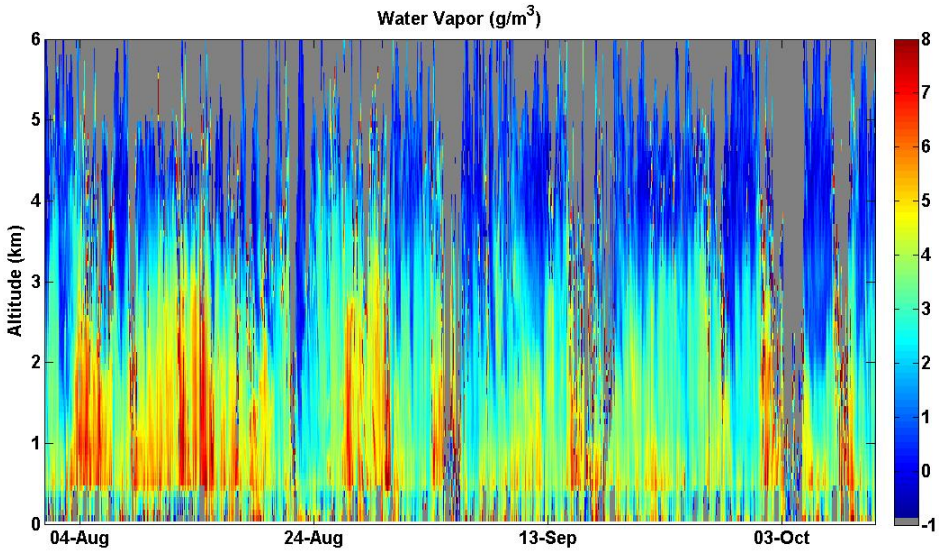

Figure 4.7: A plot of the water vapor number density from the far field channel ranging from August 1st 2015 to October 10th 2015.

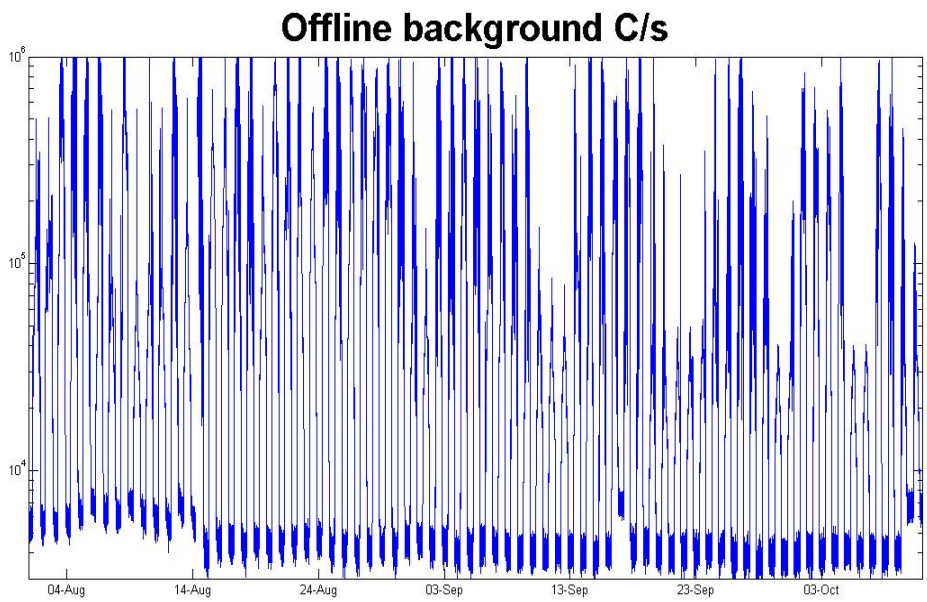

Figure 4.8: A plot of the measured offline background counts per second from the near field channel ranging from August 1st 2015 to October 10th 2015.

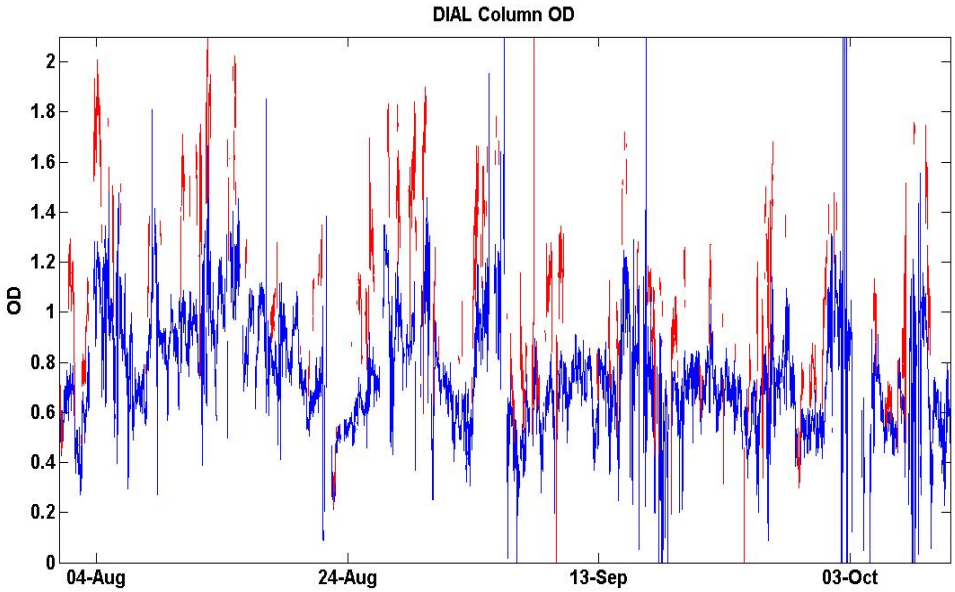

Figure 4.9: A plot of the column optical depth from the near field channel ranging from August 1st 2015 to October 10th 2015.

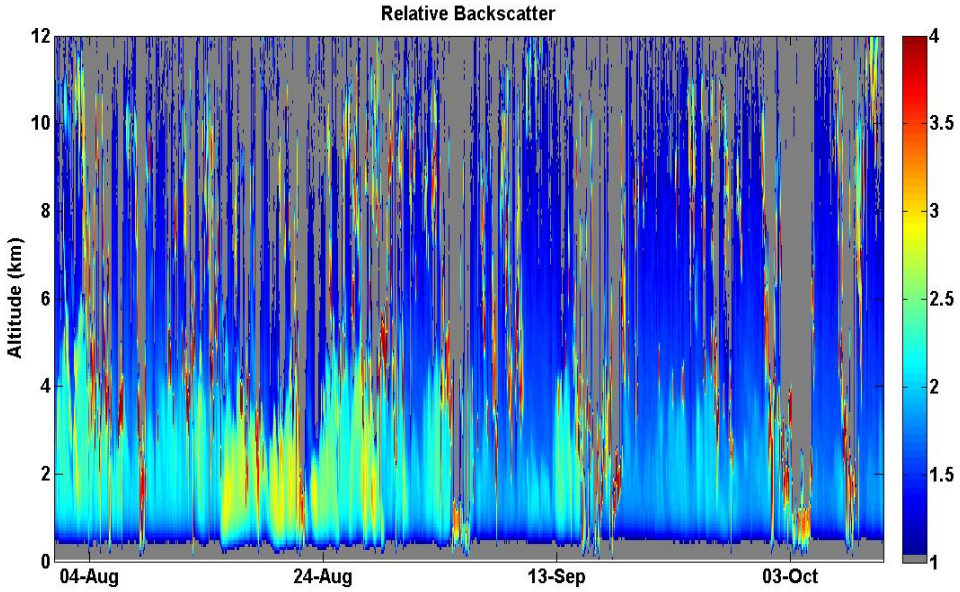

Figure 4.10: A plot of the relative backscatter from the near field channel ranging from August 1st 2015 to October 10th 2015.

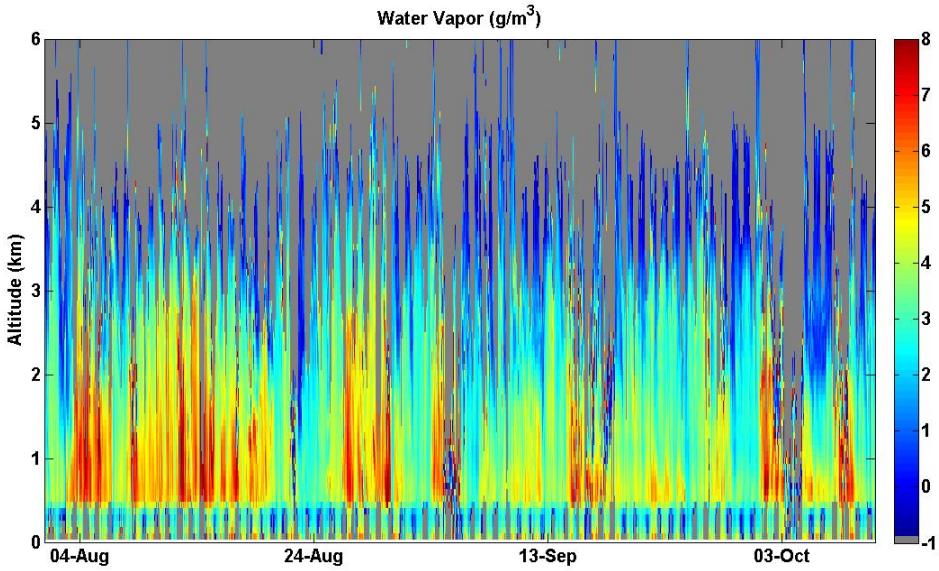

Figure 4.11: A plot of the water vapor number density from the near field channel ranging from August 1st 2015 to October 10th 2015.

These plots were chosen as providing useful information that was observed by the system noting that background counts provide information about how noisy the measurement is and that the optical depth provides information about the amount of absorption occurring from 2.5 km and 5 km.

The near field channel provides two main functions. The first is to provide relative backscatter information from lower altitudes without the requirement of an overlap function calculation. The near field channel was designed to provide full overlap starting at 600m, effectively setting the overlap function to a constant value of 1 above that range.

There is no direct measurement to easily show that the near field is operating according to its theoretical peak performance. The best way to observe the effect of the overlap function is to look at individual profiles of return counts and approximate the

location where the overlap begins to rapidly deplete the signal. This point should approximately occur at the altitude of peak signal return.

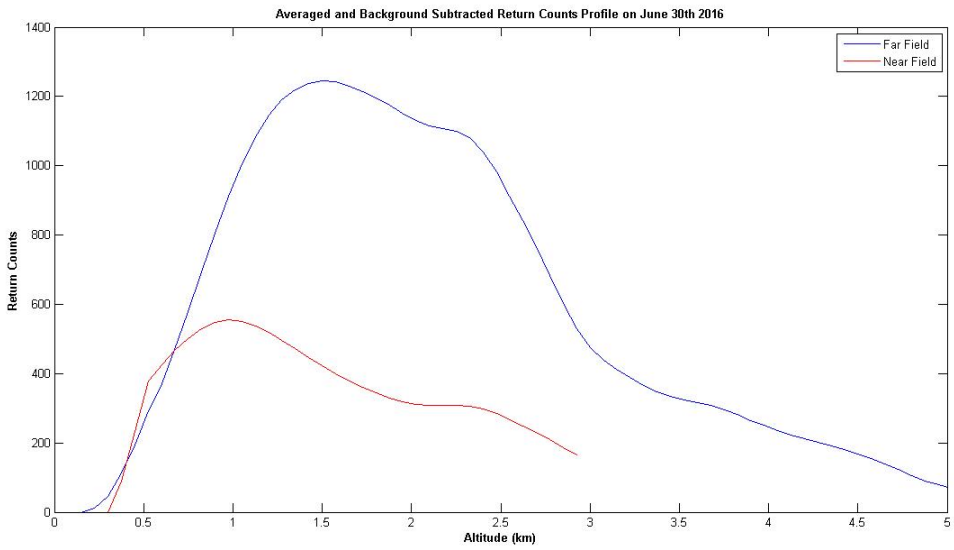

Figure 4.12: A plot from June 30th 2016 at MST 9:17am showing the far field overlap decaying below 1.5 km and the near field overlap decaying below 1 km.

We see from figure 4.12 that the near field full overlap was not achieved at our calculated theoretical distance of 600 meters. It is clear that the near field did, however, achieve a lower complete overlap than observed by the far field. Much work went into lowering the full overlap of the near field, but a solution was not found. It is of the author's opinion that the culprit may be the quality of the outgoing beam and the imperfections in the optics not meeting the assumed properties in the theory. It could also be that a more precise optical alignment is needed to lower the overlap.

The second function of the near field channel is to provide a comparison for the far field channel during alignment of the instrument. Since the overlap function falls out

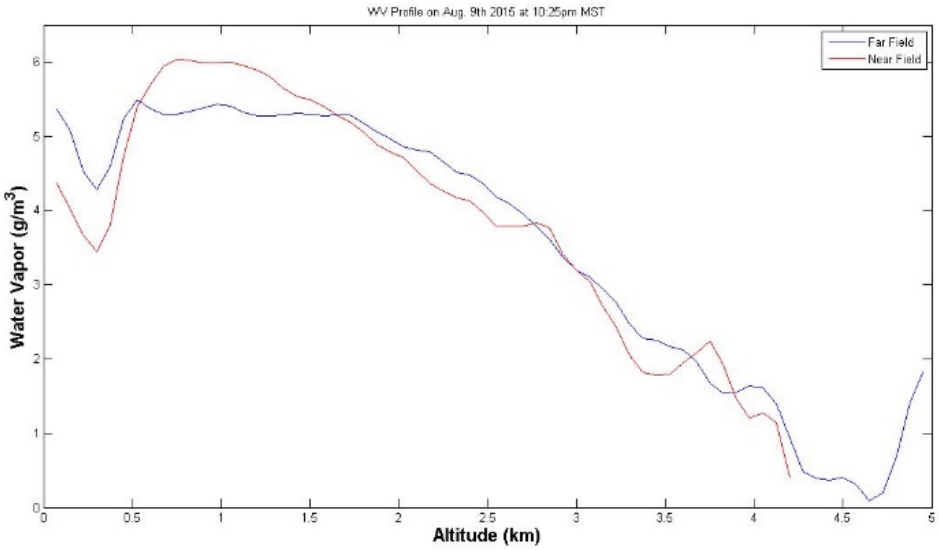

Figure 4.13: A profile from August 9th 2015 at MST 10:25pm showing good agreement between 1 km and 4.2 km. The far field continues producing reasonable data up to 5km

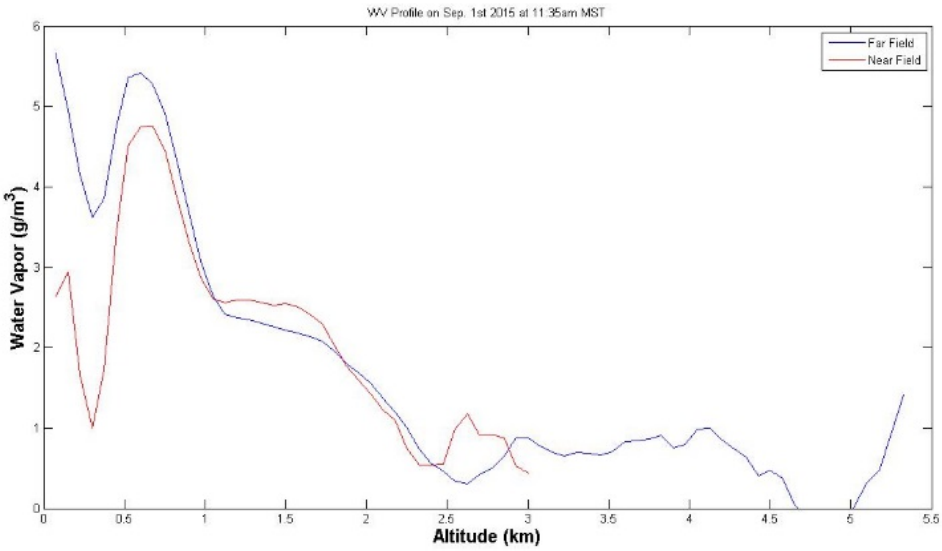

Figure 4.14: A profile from September 1st 2015 at MST 11:35am showing good agreement between 700 meters and 3 km. The far field continues producing reasonable data up to 4.7 km.

during the water vapor number density calculation, the near field and far field data should align with very close agreement. Figures 4.13 and 4.14 show two water vapor profiles from the two channels. It can be observed from these two plots that under changing conditions the two water vapor profiles are within reasonable agreement above 300 meters, averaging approximately 8% error between the near and far field channels.

CONCLUSION

An autonomous, ground based micro-pulse DIAL instrument was developed with the capability of measuring tropospheric water vapor, while obtaining aerosol profiles with complete overlap of the collected signal onto a detector ranging between 1 km and 12 km above the Earth's surface. This was achieved specifically through the modeling and development of a second detection channel within the receiver. This improvement was another step in the optimization of a water vapor DIAL instrument that was developed by the AORS laboratory at MSU [24] which was previously able to achieve full overlap between 2 km and 12 km.

The optical design of the new receiver was developed by first building a ray tracing model using the ABCD matrices method. This model was verified using Zemax, a computer based optical analysis program, to provide proof of concept. The high agreement between the two models is good evidence that the ABCD matrix analysis is a sufficient way to model and make future adjustments to the receiver as needed. This is valuable information because the ABCD matrix modeling is a very straightforward analysis technique that provides the user with a deep level of understanding regarding the effects of changes and variations that can be made to the system.

A summary of the contributions made by the author and presented in this thesis include: the analysis of a new receiver design using ABCD matrices and the verification of this ray tracing model using Zemax optical design software; the build and layout of the entire DIAL instrument into one compact, self-contained system; the alignment of the optical system; the additions and alterations to the Labview programming code needed to

run the equipment and store the measured data; the analysis of the data measured by the DIAL system.

The key improvement that was made to the system was the ability of the receiver to achieve complete overlap down to 1 km above the Earth's surface. This simplifies the normalized relative backscatter equation by setting the overlap function equal to 1 for ranges within full overlap. The overlap function for a Lidar system can vary during alignment of the receiving optics, and cannot be directly measured or accurately compensated for when the DIAL instrument is pointing up into the atmosphere. The capability to make aerosol measurements below 2 km without the correction of an overlap function holds value as a means of directly monitoring the location of the atmospheric boundary layer. This ability in combination with the water vapor measurement is useful information that climatologists and meteorologists need to push forward in understanding of the Earth's atmosphere.

The next step needed for the receiver is better filtering to improve sensitivity for daytime partly cloudy conditions. Light clouds that pass through on otherwise sunny days scatter near infrared light emitted from the sun, re-directing the light rays in every direction. The light re-directed straight down towards the earth can be collected by the DIAL telescope and is detected as noise in the return signal. Through better filtering techniques, the signal to noise ratio during these conditions can be greatly increased, offering more accurate data.

Another useful step towards the improvement of the system that would stabilize the transmitter would be the development of fiber-couple DFB laser diodes and a fiber

coupled TSOA. Reducing the first half of the transmitter to entirely fiber-coupled components would also simplify the system and reduce the spatial footprint of the instrument.

The continued improvement and optimization of this system offers a continuous alternative to the current water vapor measurement technique via weather balloon launches twice a day from weather stations around the United States. The DIAL system demonstrated within this thesis is already capable of taking continuous water vapor measurements autonomously with minimal upkeep. The longest uninterrupted data collection run presented in this thesis lasted 71 days, resulting in over 6 million “return counts vs altitude” measurements, at 10,000 pulses per measurement, gathered by the multi-channel scaler card and recorded to a computer.

Upon completion of a final maximized DIAL system, a network of these instruments can be deployed for the study of water vapor in the lower troposphere. A grid based deployment providing long-term, continuous water vapor measurement would satisfy two of the four highest priority atmospheric observations needed as reported by the National Research Council. Such a study would be integral in expanding our knowledge of weather forecasting and climate modeling, and would create a much needed platform to further the study and prediction capabilities involving the many effects that water vapor has on the atmosphere.

This work was supported under the kind auspices of the National Science Foundation grant number 1206166. Any opinions, findings, conclusions, or

recommendations found herein are those of the author and do not necessarily reflect those of NSF.

REFERENCES CITED

[1] Atkins, N. (2008, August). Vertical profile of temperature. Retrieved May 24, 2016, from Chapter 1 - The Earth and its Atmosphere: Links of interest site: http://apollo.lsc.vsc.edu/classes/met130/notes/chapter1/vert_temp_all.html

[2] Turner, DD, Feltz, WF & Ferrare, RA 2000, 'Contnuous water vapor profiles from operational ground-based active and passive sensors', *Bulletin of American Meteorological Society*, vol 81, pp. 1301-1318.

[3] Committee on Developing Mesoscale Meteorological Observational Capabilities to Meet National Needs, National Research Council, *Observing Weather and Climate from the Ground Up: A Nationwide Network of Networks,* National Academy Press, 2009.

[4] Milz, M, von Clarmann, T, Fischer, H, Glatthor, N, Grabowki, U, Hopfner, M, Kellmann, S, Kiefer, M, Linden, A, Mengistu Tsidu, G, Steck, T, Stiller, GP, Funke, B, Lopez-Puertas, M & Koukouli, ME 2005, 'Water vapor distributions measured with the Michelson interferometer for passive atmospheric sounding on board Envisat (MIPAS/Evisat)', *Jouranl of Geophysical Research* , vol 110, p. D24307.

[5] Divakarla, MG, Barnet, CD, Goldberg, MD, McMillin, LM, Maddy, E, Wolf, W, Zhou, L & Liu, X 2006, 'Validation of atmospheric infrared sounder temperatuer and water vapor retrievals with matched radiosonde measurements and forecasts', *Journal of Geophysical Research* , vol 111, p. D09S15.

[6] Russell, JM, Gordley, LL, Drayson, SR, Hesketh, WD, Cicerone, RJ, Tuck, AF, Soden, JE, Jackson, DL, Ramaswamy, V, Schwarzkopf, MD & Huang, X 2005, 'The Radiative Signature of Upper Tropospheric Moistening ', *Science* , vol 310, pp. 841-844.

[7] Feltz, WF, Smith, WL, Knuteson, RO, Revercomb, HE, and Howell, HB, 1998, ‘Meteorological Applications of Temperature and Water Vapor Retrievals from the Ground-Based Atmospheric Emitted Radiance Interferometer (AERI)’, Journal of Applied Meteorology, 37, 857-875.

[8] Guldner, J, and Spankuch, D, 2001, ‘Remote Sensing of the Thermodynamic State of the Atmospheric Boundary Layer by Ground-Based Microwave Radiometry’, Journal of Atmospheric and Oceanic Technology, 18, 925-933.

[9] Liljegren, JC, Boukabara, SA, Cady-Pereira, K, and Clough, SA, 2005, ‘The Effect of the Half-Width of the 22 GHz Water Vapor Line on Retrievals of Temperature and Water Vapor Profiles with a 12-Channel Microwave Radiometer, IEEE Transactions on Geosciences and Remote Sensing, 43, 1102-1105.

[10] Goldsmith, JE, Blair, FH, Bisson, SE & Turner, DD 1998, 'Turn key Raman lidar for profiling atmospheric water vapor, clouds, and aerosols', *Applied Optics* , vol 37, pp. 4979-4990.

[11] Eichinger, WE, Forman, PR, Griegos, J, Osborn, MA, Richter, D, Tellier, LL & Thornton, R 1999, 'The Development of a Scanning Raman Water Vapor Lidar for Boundary Layer and Tropospheric Observations', *Journal of Atmospheric and Oceanic Technology*, vol 16, pp. 1753-1766.

[12] Whiteman, DN, Melfi, SH & Ferrare, RA 1998, 'Raman lidar system for the measurement of water vapor and aerosols in the Earths atmosphere', *Applied Optics* , vol 31, pp. 3068-3082.

[13] Browell, EV, Ismail, S & Grant, WB 1998, 'Differential absorption lidar (DIAL) measurements from air and space ', *Applied Physics B*, vol 67, pp. 399-410.

[14] Rall, JA, Abshire, JB, Reusser, D & Humphrey, M 1994, 'Measurements of atmospheric water vapor using a compact AlGaAs laser based DIAL instrument', *Conference on Laser and Electro-Optics* , Washington D.C.

[15] Wulfmeyer, V 1998, 'Ground-based differential absorption lidar for water vapor and temperature profiling: Development and specifications of a high performance laser transmitter', *Applied Optics* , vol 37, pp. 3804-3824.

[16] Wulfmeyer, V & Bosenberg, J 1998, 'Ground-based differential absorption lidar for water vapor profiling: Assesment of accuracy, resolution, and meteorological applications ', *Applied Optics* , vol 37, pp. 3825-3844.

[17] Ehret, G, Fix, A, Weiss, V, Poberaj, G & Baumert, T 1998, 'Diod laser seeded parametric oscillator for airborne water vapor DIAL applications in the upper troposphere and lower stratosphere ', *Applied Physics B*, vol 67, pp. 427-431.

[18] Ehret, G, Kiemle, C, Renger, W & Simmet, G 1993, 'Airborne remote sensing of tropospheric water vapor with a near infrared differential absorption lidar system', *Applied Optics* , pp. 4634-4551.

[19] Wirth, M, Fix, A, Mahnke, P, Schwarzer, H, Schrandt, F & Ehret, G 2009, 'The airborne multi-wavelength water vapor differential absorption lidar WALES: System design and performance.', *Applied Physics B*, vol 96, pp. 201-213.

[20] Machol, JL, Ayers, T, Schwenz, KT, Koenig, KW, Hardesty R, M, Senff, CJ, Krainak, MA, Abshire, JB, Bravo, HE & Sandberg, SP 2004, 'Preliminary measurements with an automated compact differential absorption lidar for profiling water vapor', Applied Optics , vol 43, pp. 3110-3121.

[21] Nehrir, AR, Repasky, KS, Carlsten JL, Obland, MD , and Shaw, JA, 2009, 'Water Vapor Profiling using a Widely Tunable, Amplified Diode Laser Based Differential Absorption Lidar (DIAL)', Journal of Atmospheric and Oceanic Technology, Vol. 26, No. 4, 733–745.

[22] Nehrir, AR 2008, 'Water vapor profiling using a compact widely tunable diode laser differential absorption lidar (DIAL)', Thesis, Electrical and Computer Engineering , Montana State University , Bozeman.

[23] Nehrir, AR, Repasky, KS & Carlsten, JL 2011, 'Eye-Safe Diode-Laser-Based Micropulse Differential Absorption Lidar (DIAL) for Water Vapor Profiling in the Lower Troposphere', Journal of Atmospheric and Oceanic Technology , vol 28, pp. 131-147.

[24] Nehrir, AR, 2011 'Development of an eye-safe diode-laser-based micro-pulse differential absorption lidar (MP_DIAL) for atmospheric water vapor and aerosol studies', Dissertation, Electrical and Computer Engineering , Montana State University , Bozeman.

[25] Didier Bruneau, Philippe Quaglia, Cyrille Flamant, and Jacques Pelon, "Airborne lidar LEANDRE II for water-vapor profiling in the troposphere. II. First results," Appl. Opt. 40, 3462-3475 (2001)

[26] Rothman et al., LS 2003, 'The HITRAN molecular spectroscopic databse: edition of 2000 including updates through 2001', *Journal of Quantatative Spectroscopy and Radiative Transfer*, vol 82, no. 1-4, pp. 5-44.

[27] Weckwerth, Tammy M., et al. "An overview of the International H2O Project (IHOP_2002) and some preliminary highlights." *Bulletin of the American Meteorological Society* 85.2 (2004): 253.

[28] Wulfmeyer, Volker, et al. "The Convective and Orographically-induced Precipitation Study (COPS): the scientific strategy, the field phase, and research highlights." *Quarterly Journal of the Royal Meteorological Society* 137.S1 (2011): 3-30.

[29] Reagan, J. A., T. W. Cooley, and J. A. Shaw, 1993: Prospects for an economical, eye safe water vapor lidar. *Proc. Int. Geoscience and Remote Sensing Symp.*, Tokyo, Japan, IEEE, 872–874.

[30] Reagan, J. A., H. Liu, and J. F. McCalmont, 1996: Laser diode based new generation lidars. *Proc. Int. Geoscience and Remote Sensing Symp.*, Lincoln, NE, IEEE, 1535–1537.

[31] R. M. Measures. Laser remote sensing: Fundamentals and applications. Strona 510, 1984

[32] Repasky, K.S.; Moen, D.; Spuler, S.; Nehrir, A.R.; Carlsten, J.L. Progress towards an Autonomous Field Deployable Diode-Laser-Based Differential Absorption Lidar (DIAL) for Profiling Water Vapor in the Lower Troposphere. *Remote Sens.* 2013, *5*, 6241-6259.

[33] Vidler, M & Tennyson, J 2000, 'Accurate partition function and thermodynamic data for water', *Journal of Chemical Physics*, vol 113, no. 21, pp. 9766-9771.

[34] Browell, EV, Ismail, S & Grossman, BE 1991, 'Temperature sensitivity of differential absorption lidar measurements of water vapor in the 720 nm region', *Applied Optics* , vol 30, pp. 1517-1524.

[35] "Calculation of Molecular Spectra with the Spectral Calculator." *Spectral Calc*. GATS Inc. Web. 15 June 2016. <http://www.spectralcalc.com/info/CalculatingSpectra.pdf>.

[36] Wulfmeyer, V & Walther, C 2001, 'Future performance of ground-based and airborne water-vapor differential absorption lidar. I. Overview and theory', *Applied Optics*, vol 40, no. 30, pp. 5304-5320.

[37] Bosenberg, J 1998, 'Ground-based differential absorption lidar for water-vapor profiling: methodology', *Applied Optics*, vol 37, pp. 3845-3860.

[38] Richard Phelan, Michael Lynch, John F. Donegan, and Vincent Weldon, "Absorption line shift with temperature and pressure: impact on laser-diode-based H_2O sensing at 1.393 µm," Appl. Opt. 42, 4968-4974 (2003)